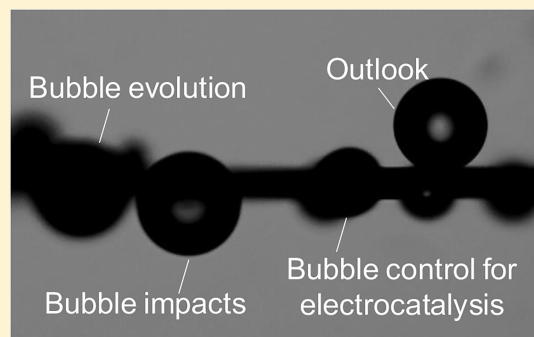


Gas Bubbles in Electrochemical Gas Evolution Reactions

Xu Zhao,[†] Hang Ren,[‡] and Long Luo^{*,†}[†]Department of Chemistry, Wayne State University, Detroit, Michigan 48202, United States[‡]Department of Chemistry and Biochemistry, Miami University, Oxford, Ohio 45056, United States

ABSTRACT: Electrochemical gas evolution reactions are of vital importance in numerous electrochemical processes including water splitting, chloralkaline process, and fuel cells. During gas evolution reactions, gas bubbles are vigorously and constantly forming and influencing these processes. In the past few decades, extensive studies have been performed to understand the evolution of gas bubbles, elucidate the mechanisms of how gas bubbles impact gas evolution reactions, and exploit new bubble-based strategies to improve the efficiency of gas evolution reactions. In this feature article, we summarize the classical theories as well as recent advancements in this field and provide an outlook on future research topics.



INTRODUCTION

Electrochemical gas evolution reactions have been widely regarded as the crucial reactions in energy conversion and storage systems. These reactions include the oxygen evolution reaction (OER) and hydrogen evolution reaction (HER) in water-splitting electrolyzers, the chlorine evolution reaction (CER) in the chloralkaline process, the hydrazine oxidation reaction (HzOR) in fuel cells, and the CO₂ reduction reaction (CO₂RR) for regenerating fuels.^{1–10} During these gas evolution processes, triple-phase boundaries (i.e., electrode/gas/electrolyte interfaces) constantly form as a result of bubble evolution, which has significant impacts on the processes at electrodes. To accelerate the kinetics of electron transfer reactions and overcome the overpotential associated with the gas evolution reactions, it is essential to understand the dynamics of electrode/gas/electrolyte interfaces and how gas bubble behaviors influence this interface.

During the past few decades, extensive studies have been performed on interfacial bubbles, including their generation and detection, as well as the mechanisms of bubble nucleation, formation, and stabilization.¹¹ For example, the formation of nanobubbles has been investigated using the quartz crystal microbalance,¹² attenuated total internal reflection infrared spectroscopy,¹³ and potential/current fluctuations.¹⁴ Moreover, high-speed photography,¹⁵ in situ transmission electron microscopy,¹⁶ atomic force microscopy,¹⁷ single-molecule fluorescence microscopy,^{18,19} and dark field microscopy^{20,21} have been employed to study the dynamics of gas bubbles. Some of these work on nanobubbles are covered in a recent special issue of *Langmuir*.²² Because interfacial properties including surface forces, lubrication, and adsorption behaviors can be altered by gas bubbles, systematic investigation of these interfacial bubble behaviors, especially in the context of gas-evolving electrodes, represents an efficient avenue for

modulating the interfacial reaction process and improving the efficiency of electrocatalysis.

In this feature article, we first revisit the bubble dynamics at gas-evolving electrodes including nucleation, growth, coalescence, and detachment. Then, we summarize the impact of gas bubbles on different aspects of a gas evolution system including interfacial supersaturation, surface coverage, ohmic resistance, mass transfer, and catalyst stability. After that, we present the newly developed bubble-based strategies for achieving high-efficiency gas-evolving electrocatalysis. At the end, we provide an outlook on potential future research topics in this field.

HOW DO GAS BUBBLES EVOLVE?

The life cycle of a bubble at a gas-evolving electrode typically comprises four stages: nucleation, growth, coalescence, and detachment. Nucleation is the stochastic formation of a cluster of gas molecules from a solution supersaturated with dissolved gas. After nucleation, the bubble continues to grow by taking up more dissolved gas molecules. As the bubble grows, the buoyant force on the bubble increases. When the buoyant force is strong enough to counter the adhesion force that keeps the bubble on the electrode surface, the bubble is lifted and then detaches from the electrode surface. Coalescence occurs when two bubbles are in contact, either on the electrode or in the solution, to reduce the overall surface energy. In this section, we briefly revisit these bubble dynamics during electrochemical gas evolution reactions.

Nucleation. Nucleation is the first step of bubble formation, commonly described by classical nucleation theory.^{23,24} As schematically shown in Figure 1, the free energy required to form a bubble in solution is the sum of the

Received: January 12, 2019

Revised: March 10, 2019

Published: March 19, 2019

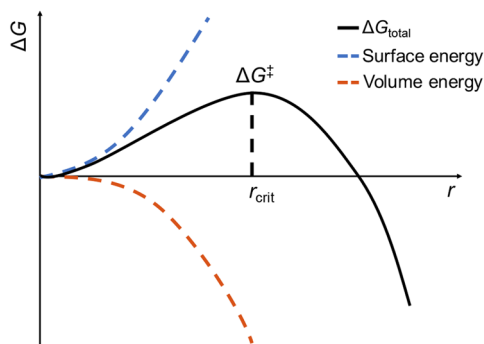


Figure 1. Contribution of surface energy (blue line) and volume energy (orange line) to the total free energy for bubble formation in classical nucleation theory. The maximum total free energy, ΔG^\ddagger , corresponds to the activation energy for bubble nucleation, which occurs at a critical bubble radius, r_{crit} . A bubble with a larger radius than the critical nucleus is energetically favorable to growth, whereas a bubble with a smaller radius than the critical nucleus is energetically favorable to dissolution.

surface energy for forming a gas–liquid interface and the volume energy for forming a bulk gas phase. The energy cost for forming the gas–liquid interface increases with the interfacial surface area and, more specifically, is approximately proportional to the square of the bubble radius. On the contrary, forming a bulk gas phase from a supersaturated solution is energetically favorable. The corresponding volume energy change is proportional to the cube of the bubble radius. A free-energy barrier arises for bubble formation as a result of the opposite direction of the change in volume energy and surface energy with regard to bubble radius. The peak value of this energy barrier corresponds to the activation energy for bubble nucleation, which occurs at a critical bubble radius (r_{crit}). By substituting this activation energy into the Arrhenius equation, we can obtain the rate equation:²⁵

$$J = J_0 \exp\left(-\frac{16\pi\gamma^3\Phi(\theta)}{3k_B T(P_{\text{gas}} - P_0)^2}\right) \quad (1)$$

In this equation, J_0 is the pre-exponential factor, γ is the surface tension, $\Phi(\theta) = (2 - \cos\theta)(1 + \cos\theta)^2/4$ is a geometric factor, which is a function of the contact angle (θ) of the critical nucleus on the surface, k_B is Boltzmann's constant, T is temperature, P_{gas} is the partial pressure of gas in the bubble, and P_0 is the ambient pressure. It can be seen from eq 1 that the nucleation rate, J , is strongly affected by P_{gas} . According to Henry's law, P_{gas} is proportional to the concentration of dissolved gas. Altogether, it indicates that a certain supersaturation level of dissolved gas is needed to reach a reasonable nucleation rate.

Numerous efforts have been made to measure the supersaturation level of dissolved gas required for bubble nucleation at gas-evolving electrodes. However, there has been considerable variation in the reported values. Bon,²⁶ Shibata,²⁷ and Eckert²⁸ separately measured the supersaturation required for H_2 bubble nucleation on Pt electrodes during HER and found that it ranged from 20 to 160. Such a discrepancy might arise from the different numbers and properties of nucleation sites on their electrodes. For example, Westerheide and Westwater²⁹ have observed that H_2 bubbles were formed repetitively from the same sites where scratches or crevices

existed. Please note that there are also many studies on the supersaturation level of dissolved gas for homogeneous bubble nucleation in solution,³⁰ but they are beyond the scope of this feature article and are not discussed here.

To overcome the complexity of multiple bubble nucleation events at the gas-evolving electrode, White and co-workers^{14,25} recently developed a nanoelectrode-based method. Unlike conventional macroelectrode measurements, the nanoelectrode-based method can reduce the number of bubbles nucleating at the electrode to unity, making it a single-entity electrochemical measurement method for bubbles. Moreover, steady-state concentration profiles of the reactant and product are readily achieved as a result of the fast mass transfer toward and away from the nanoelectrode, making the supersaturation measurement accurate.³¹ Single H_2 , N_2 , and O_2 nanobubbles have been demonstrated to be electrochemically generated from proton reduction, hydrazine oxidation, and hydrogen peroxide oxidation, respectively.^{14,32–37} As shown in Figure 2A,B, during the cathodic sweep of the nanoelectrode

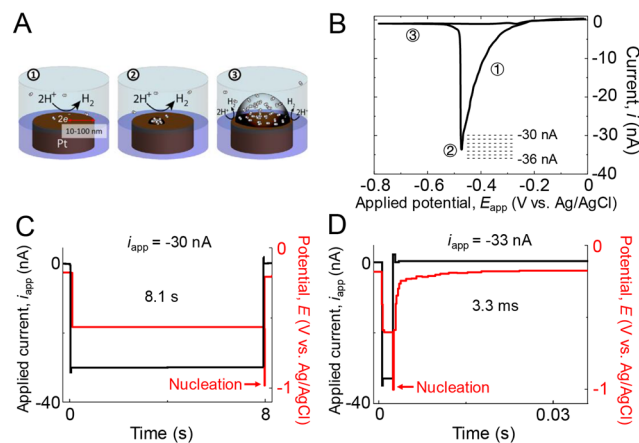


Figure 2. (A) Illustration of electrochemical nucleation of a single bubble from proton reduction using a nanoelectrode. The corresponding (B) cyclic voltammogram and (C and D) potential–time traces (red) and current–time traces (black) under galvanostatic control. Reproduced from ref 25, copyright 2018 by the American Chemical Society.

potential, the current increases until the dissolved H_2 concentration at the electrode is sufficiently high for bubble nucleation. After nucleation, the bubble grows and covers nearly the entire surface of the nanoelectrode, causing an immediate current drop. Further negative scan of the electrode potential does not result in any notable changes in the current. This stable low-current level after bubble formation was explained by steady-state equilibrium at the electrode surface, where the outflux of H_2 from the bubble into its surrounding solution is balanced by the influx of H_2 generated at the gas–liquid–electrode three-phase boundary.³⁸ The peak current (i_p) is used to calculate the concentration of dissolved gas required for nucleation

$$i_p = 4nFD(C - C_{\text{bulk}})a \quad (2)$$

where n is the number of electrons transferred per H_2 formed, F is Faraday's constant, D is the diffusion coefficient of the dissolved gas, a is the electrode radius, and C and C_{bulk} are the concentrations of dissolved gas on the electrode surface and in the bulk electrolyte, respectively. It has been found that the

concentrations required for nucleating gas bubbles at different Pt electrodes are consistent: 0.23 ± 0.02 M for H_2 ,¹¹ 0.11 ± 0.01 M for N_2 ,³⁴ and 0.24 ± 0.04 M for O_2 ,³⁵ all of which correspond to the supersaturation level of a few hundred. In the follow-up studies by Luo and co-workers,^{36,37} they have demonstrated that the supersaturation level for H_2 bubble nucleation is also insensitive to the metallic electrode materials, including Pt, Au, and Pd.

To gain further insight into the energetics of bubble nucleation, White and co-workers²⁵ measured the nucleation rate of individual H_2 nanobubbles under different supersaturation levels of dissolved H_2 . As discussed above, the nucleation rate is a function of the concentration of dissolved H_2 on the electrode surface, which can be adjusted by applying different currents according to eqs 1 and 2. Experimentally, the nucleation rate was estimated from the induction time for nucleation because they are numerical inverses. To assess the bubble nucleation rates, galvanostatic measurements at different currents were conducted. As the current was stepped to a constant value, the potential showed a rapid increase, indicating the start of the HER. After a certain period, the potential showed another rapid increase, which was attributed to the blocked H^+ transport by the generated bubble. The induction time for bubble generation can be recorded as the current was switched back to zero. As shown in Figure 2C,D, the nucleation events are indicated by the abrupt potential increase (red arrows). The nucleation rate was measured to increase by ~ 3 orders of magnitude (induction time from 8.1 s to 3.3 ms) with only an $\sim 10\%$ increase in dissolved-gas supersaturation (the HER current from 30 to 33 nA). The nucleation of H_2 bubbles was found to be heterogeneous with a contact angle of $\sim 150^\circ$ for the critical bubble nuclei on the electrode surface, which was determined by fitting eq 1. A similar heterogeneous nucleation mechanism has also been found for O_2 bubbles.³⁹ The experimental results from the nucleation studies using nanoelectrodes can be well described by classical nucleation theory. However, it should be noted that for solids and crystals, nucleation mechanisms are more complicated than that described by classical nucleation theory, where multiple steps and a prenucleus are involved.^{40,41} The complicated nucleation mechanisms seem less pronounced for bubble nucleation at gas-evolving electrodes.

Growth. After nucleation, gas bubbles continue to grow, driven by the higher internal pressure of the bubbles than the Laplace pressure and the flux of dissolved gas into bubbles.^{42,43} Three possible modes of bubble growth have been identified:⁴² inertia-controlled growth, diffusion-controlled growth, and “direct injection” growth. Bubble growth can be generally described by an empirical equation, $R(t) = At^\beta$, where $R(t)$ is the bubble radius, β is the growth coefficient, and A is a proportionality constant. Inertia-controlled growth occurs initially but lasts only a very short time (~ 0.01 s) before the transition to the diffusion-controlled mode.⁴² In the inertia-controlled growth mode, bubble growth is governed by the momentum interaction between the bubble and ambient fluid with a value of $\beta = 1$. The later stage of bubble growth is controlled by the diffusion of dissolved gas into the bubble, and $\beta = 0.5$ is expected.⁴⁴ The third growth mode, direct injection, means that all of the gas species are directly injected into a bubble. The growth of the radius is $R \approx t^{1/3}$, or $\beta = 1/3$. This growth mode has been observed for H_2 and O_2 bubbles on electrodes at high current densities.⁴² Bubble growth on electrodes has also been studied under microgravity,⁴⁵

magnetic fields,⁴⁶ and flow.⁴⁷ These previous studies on bubble growth mostly relied on conventional analytical techniques and tools, so little is known about the initial bubble growth from nuclei due to the short time scale and small dimension. Note that bubble growth requires a gas-supersaturated solution; otherwise, a bubble undergoes the dissolution process, which can occur in certain situations, most obviously when no current is applied at the gas-evolving electrode.⁴⁸

Coalescence. When two bubbles come into close proximity to each other, they can merge into a single bubble via coalescence. The driving force for coalescence is the decrease in surface energy from the reduced total area of the gas–liquid interface. The coalescence process was found to depend on many factors, including the concentration of salts as well as the specific combination of cations and anions in the electrolyte.^{49–53} With the development of advanced high-speed optical microscopy, the coalescence process has become more evident than before. As shown in Figure 3,⁵⁴ the coalescence

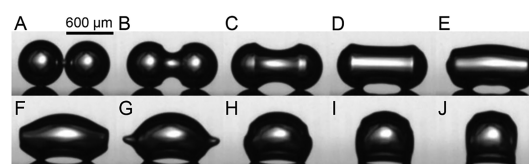


Figure 3. High-speed images of two 300- μm -radius bubbles during coalescence. The images are separated from each other by 75 μs . (A–D) Neck formation. (E–J) Propagation of the capillary wave. Reproduced with permission from ref 54, copyright 2018 by Cambridge University Press.

process starts by pushing away the liquid layer between the two bubbles, from which a thin liquid film is formed as a collapsing neck. Further thinning of the liquid film leads to the rupture at a critical thickness (< 100 nm). The collapsing neck propagates and oscillates as a surface capillary wave. The formation of the neck is dominated by viscosity within the first 10 ns upon touching and then crosses over to an inertia-dominated process.⁵⁵ The propagation and oscillation dynamics during bubble coalescence can be simulated using a boundary integral code as demonstrated by Lohse and co-workers,⁵⁴ which shows good agreement with the experimental data.

Detachment. Bubble detachment is of great importance to gas evolution processes because it re-exposes the active area that was previously blocked by attached bubbles. During bubble detachment, the three-phase contact line of a bubble is typically pinned to the substrate, which is followed by necking between the bubble and substrate as shown in Figure 4.^{56,57} Further narrowing of the bubble neck leads to bubble

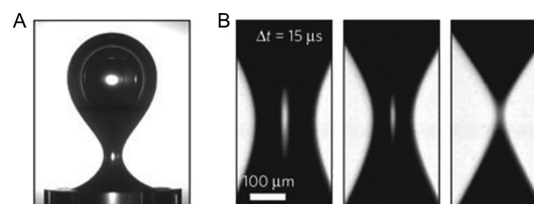


Figure 4. (A) Image of a detaching bubble. (B) Close-up images of the bubble neck, each separated by 15 μs , before disconnection. Reproduced with permission from ref 57, copyright 2009 Springer Nature Publishing.

detachment from the substrate. In addition to high-speed imaging, electrochemical noise analyses of the current, resistance, and potential have also been utilized to study the dynamics of bubble detachment from electrodes during gas evolution reactions.^{58,59}

In the most simplified model, bubble detachment is caused by the buoyant force overcoming the adhesion force on a bubble. For a bubble detaching from a horizontal substrate, the theoretical bubble radius at detachment, R_F , at which buoyant and adhesion forces are in balance, can be derived as⁵⁶

$$R_F = \left(\frac{3 \gamma R_p}{2 \rho g} \right)^{1/3} \quad (3)$$

In this equation, γ is the surface tension, ρ is the density of the liquid, g is the gravitational constant, and R_p is the radius of the pinning area. The equation was derived by assuming a spherical cap geometry of a bubble on the electrode surface and only the buoyant and adhesion forces on the bubble. A modified version of eq 3, taking the geometry of the bubble's contact line into account, was discussed by Lohse, Zhang, and co-workers.⁶⁰ For a bubble detaching from a vertical wall, the force balance analysis is more complex than that for a bubble detaching from a horizontal substrate. Because the bubble shape is not axisymmetrical, the buoyant force on the bubble has two components, one is perpendicular to the wall and the other one is parallel. Meanwhile, the adhesion force is not constant over the circumference due to the variation in the contact angles. As a result, it is difficult to mathematically derive the analytical expression of R_F for bubbles detaching from a vertical wall.⁶¹

In addition to the buoyant force and adhesion force, the electrostatic force between the charged bubble and electrode surface also plays an essential role in determining the R_F .⁶² The bubble surface charge was found to be a function of solution pH, typically being positive at pH < 2 and negative at pH > 3.⁶² The negative bubble surface charge at normal pH values is believed to arise from the preferential adsorption of OH⁻ ions at the gas/water interface, possibly under the influence of a small net orientation of H₂O dipoles at the surface with positive ends toward the solution.⁶³ Electrode surface charge, on the other hand, depends on the applied potential and the potential of zero charge of the electrode material.⁶⁴ The effect of the electrostatic interaction on bubble detachment is manifested by the different detachment behaviors at different pH values. The radii of detached H₂ bubbles are larger at low pH compared to those at high pH. At low pH, the positively charged H₂ bubbles and the negatively charged electrode result in an attractive electrostatic force that needs to be overcome in addition to the adhesion force, leading to larger detachment radii of H₂ bubbles.⁶² The same electrostatic effect has been observed for the detachment of O₂ and Cl₂ bubbles from gas-evolving electrodes.⁶² Other factors such as the Marangoni stress,⁶⁵ surfactants,⁶⁶ and magnetic field^{67–69} have also been studied for their influence on bubble detachment.

■ WHAT ARE THE IMPACTS OF GAS BUBBLES ON A GAS EVOLUTION REACTION?

Electrogenerated gas bubbles have a strong influence on a gas evolution reaction. Ever since nucleation, gas bubbles have started to affect the concentration level of their dissolved form by an equilibrium at the gas/electrolyte interface. In the meantime, these gas bubbles can also block the electrode

surface. As bubbles grow, coalesce, and detach from the electrode, they effectively stir the electrolyte solution and alter the mass transfer of reactants and products. After departure from the electrode, the generated bubbles could considerably change the solution path through the electrolyte, causing electrolyte ohmic resistance. All of the bubble dynamics can potentially cause electrode damage as well.^{16,70} Experimental and theoretical investigations on the impacts of electro-generated bubbles started in the 1960s^{29,71,72} but are ongoing as a result of their complexity and importance. In this section, we will present some classical theories as well as recent advancements related to the impact of gas bubbles on gas evolution reactions with respect to the following factors: interfacial supersaturation, surface coverage, ohmic resistance, mass transfer, and catalyst stability.

Interfacial Supersaturation. During gas evolution processes, the electrolyte solution near electrodes is supersaturated with dissolved gas. The interfacial supersaturation level can reach as high as 300 to 400.^{11,14,32,33,36,37} According to the Nernst equation, such a high local concentration of the product (in this case, dissolved gas) on the electrode surface causes a concentration overpotential (η_c), which is expressed as^{73,74}

$$\eta_c = -\frac{RT}{nF} \ln \frac{C_g}{C_g^{\text{sat}}} \quad (4)$$

where n is the number of electrons transferred to form one gas molecule, C_g is the interfacial concentration of dissolved gas at the electrode, and C_g^{sat} is the saturation concentration of gas at 1 atm pressure. The basic mass-transfer equation relates C_g to the current density (j) as

$$\frac{j}{nF} = k(C_g - C_{\text{bulk}}) \quad (5)$$

where k is the mass-transfer coefficient of dissolved gas and C_{bulk} is the dissolved gas concentration in the bulk solution.

At low current densities, k is dominated by the diffusion of dissolved gas and thus stays relatively constant. C_g increases with current density and reaches its maximum value when a bubble nucleates. Hence, the theoretical maximum η_c can be estimated to be ~70 mV for the hydrogen evolution reaction ($n = 2$) and ~35 mV for the oxygen evolution reaction ($n = 4$) from eq 4 using the experimentally measured supersaturation level of ~300 required for H₂ and O₂ gas bubble nucleation.^{14,33}

At high current densities, gas bubbles begin to evolve at the electrode. C_g becomes a more complex function of current density compared to that at low current densities because k has a significant contribution from bubble-caused convective mass transfer, which depends on the current density. Dukovic and Tobias⁷³ carried out a numerical study of the influence of attached bubbles on the interfacial supersaturation using the model in Figure 5A. In this model, they set the dissolved-gas concentration beyond the boundary layer (the boundary layer is colored) and at the bubble/electrolyte interface to the gas solubility. During gas evolution reactions, the bubble attached to the electrode then acts as a sink drawing the dissolved gas from the supersaturated surrounding electrolyte. The concentration of dissolved gas, C_g , is significantly lower near the bubble contact area as compared to that further away (Figure 5B). As a result, the presence of attached bubbles could

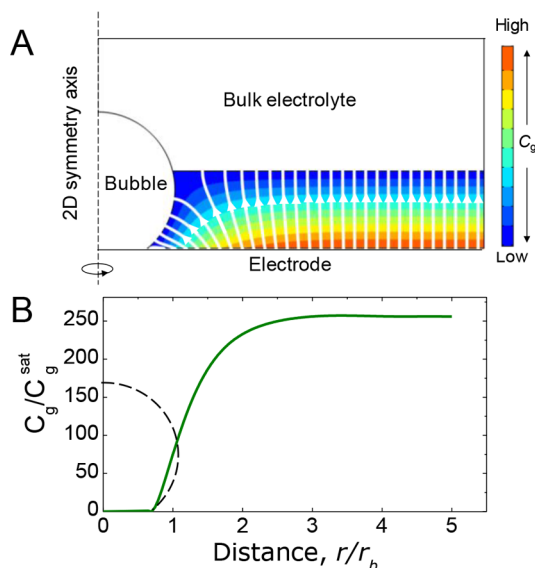


Figure 5. (A) Geometric configuration of the attached bubble model used by Dukovic and Tobias. The color contour schematically shows the concentration distribution of dissolved gas in the boundary layer. The white lines highlight the flux of dissolved gas. (B) Supersaturation level of dissolved gas at the electrode surface vs the distance from the center of the attached bubble normalized by the bubble radius (r/r_b). Adapted with permission from ref 73, copyright 1987 by the Electrochemical Society.

decrease the overall cell voltage for water electrolysis by locally lowering the concentration overpotential.

Vogt has also derived a theoretical expression of C_g for gas-evolving electrodes based on a different mass transfer model in which he considered the macroconvection past the electrode and the microconvection caused by the attached bubbles on the electrode.^{74,75} The macroconvective mass transfer is the mass transfer influenced by the liquid flow parallel to the electrode surface, which is not related to events directly connected to gas evolution.⁷⁵ In comparison, microconvective mass transfer is caused by the bubble growth at the electrode pushing away the liquid in the vicinity of the adhering bubble, resulting in a periodic disturbance of the diffusion layer with an increase in mass transfer. For the unstirred solution, the concentration overpotential was found to increase with increasing current density and reach a plateau of ~ 65 mV. At high current densities ≥ 100 mA/cm², the efficient bubble-induced mass transfer at the electrode prevented the local supersaturation level from increasing further, leading to a plateau of concentration overpotential. A similar trend in the concentration overpotential was observed for the stirred electrolyte. A comparison of the calculated concentration overpotential by Vogt and the experimental data obtained by Shibata shows good agreement.⁷⁴ These results suggest that the interfacial supersaturation of dissolved gas can also be reduced by bubble-induced micro/macroconvection. Although Vogt studied the influence of bubbles on interfacial supersaturation from a different perspective compared to that of Dukovic and Tobias, they arrived at a similar conclusion: the formation of gas bubbles reduces the concentration overpotential.

Surface Coverage. Attached bubbles are known to cause unfavorable mass transport and ohmic and kinetic effects due to the blockage of catalytic sites.^{76,77} Before elaborating on

these effects, we begin with a brief discussion of the bubble coverage of electrodes (Θ),^{78,79} which is defined as the fraction of an electrode surface covered by attached bubbles. Numerous experimental investigations have been conducted to obtain information on how bubble coverage varies with current density.^{47,80–83} A typical experiment for measuring bubble coverage involves the use of a camera to record the bubble population and the diameters of adhering bubbles. Figure 6

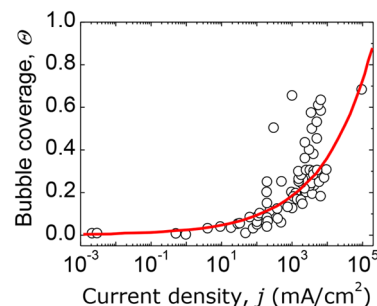


Figure 6. Bubble coverage on an electrode surface (Θ) as a function of current density for gas evolution reactions in stagnant electrolyte at ambient temperature. Reproduced with permission from ref 79, copyright 2005 by Elsevier.

shows a collection of data obtained in stagnant electrolyte (electrolyte without flow and with unhindered bubble release), summarized by Vogt.⁷⁹ The bubble coverage increases nonlinearly with the current density (j) as expressed by an empirical relationship

$$\Theta = \left(\frac{j}{j_{\Theta \rightarrow 1}} \right)^{0.3} \quad (6)$$

where $j_{\Theta \rightarrow 1}$ is the current density at nearly full bubble coverage. Equation 6 is a simple equation relating the bubble coverage to the current density in the stagnant electrolyte. Besides current density, several other parameters can also affect the coverage in practical applications, including the surface state and wettability of electrodes,^{78,79} the composition and flow velocity of electrolyte,^{47,83,84} temperature, reaction time,⁷⁹ and pressure.^{85,86} An analysis of these parameters indicates that bubble coverage is essentially affected by three quantities:⁸⁵ (1) the rate of gas evolution at the electrode, (2) the residence time of bubbles on the electrode, and (3) the size of bubbles when they detach.

As mentioned above, attached bubbles exert two other effects on the electrode potential besides the concentration overpotential: (1) inducing ohmic obstruction within the electrolyte (ohmic effect) and (2) masking the electrode surface, which increases the activation overpotential by increasing the effective current density (kinetic effect).⁷³ Accordingly, the total overpotential associated with attached bubbles can be written as^{77,87}

$$\eta = \eta_{\text{ohm}} + \eta_a + \eta_C \quad (7)$$

where subscripts ohm, a, and C stand for ohmic, activation, and concentration, respectively.

In the previous section, we reviewed how the presence of bubbles can lower the concentration overpotential. Now, we continue discussing the other two terms in eq 7. Sides and Tobias⁸⁸ theoretically analyzed the potential and current distributions around a spherical bubble tangent to an electrode

considering only the ohmic effect. They found if these bubbles were 3 bubble diameters apart from each other and the bubble diameter was $1/10$ of the interelectrode gap in parallel planar cell geometry, the increment of resistance (ΔR) caused by these attached bubbles was a 1% increase in resistance. When bubbles are close-packed at the electrode, the resistance increase is at least 8% for the same cell geometry.^{88,89}

A simple model for understanding and quantifying the kinetic effect is based on the effective area available to the current.⁸⁷ The Tafel equation relates the current density (i/A) and kinetic overpotential (η_0) on a given smooth surface in the absence of gas bubbles by Tafel constants a and b :

$$\eta_0 = a + b \log\left(\frac{i}{A}\right) \quad (8)$$

The presence of attached bubbles reduces the superficial electrode area, A , to the effective electrode area, A_{eff} yielding the expression of activation overpotential, η_a , due to the increased effective current density.

$$\eta_a = b \log\left(\frac{A}{A_{\text{eff}}}\right) \quad (9)$$

Along with theoretical considerations, experimental work has also been attempted by several groups to estimate each component of the total overpotential.^{76,77,90} Figure 7A shows

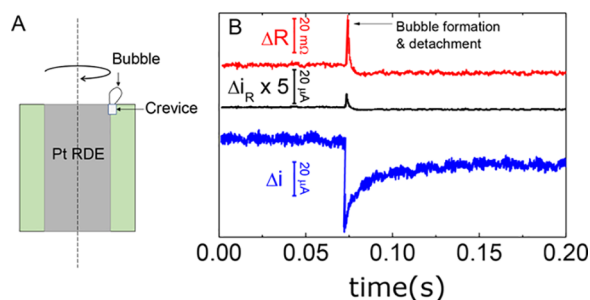


Figure 7. (A) Experimental design for estimating different types of overpotentials associated with bubble formation during hydrogen evolution. A small crevice was intentionally created at the edge between metal and the insulating resin on a Pt rotating disk electrode (RDE) serving as a preferred site for forming a single H_2 bubble. (B) Fluctuation of electrolyte resistance (ΔR), ohmic current (Δi_R), and total current (Δi) during the formation and detachment of an electrogenerated H_2 bubble. Adapted with permission from ref 76, copyright 2005 by Elsevier.

the experimental design developed by Huet and co-workers.⁷⁶ They created an artificial preferential site for bubble nucleation during the hydrogen evolution reaction at the border of a Pt rotating disk electrode: a small crevice in the insulating resin. At such a site, heterogeneous nucleation triggers bubble production at a level of gas supersaturation lower than at other sites on the electrode. The rotating disk electrode was placed upward to facilitate bubble detachment under the action of buoyancy and shear force. This experimental design favors the eruption of a reproducible isolated single bubble from this artificial discontinuity. Figure 7B shows the fluctuation of measured electrolyte resistance (ΔR), ohmic current (Δi_R), and total current (Δi) during the generation and departure of a H_2 bubble. The quick positive jump (in about 3 ms) in the $\Delta R-t$ trace corresponds to the blockage of the electrode surface by a growing bubble. As the bubble leaned out of the

electrode and was finally ejected under the action of shear forces, the screened surface was released, leading to the electrolyte resistance decrease, with the residence time of bubble on the metallic surface being approximately 25 ms. The expected decrease in current due to the ohmic effect (Δi_R) is proportional to ΔR . However, the observed total current, Δi , increased by a much larger (>20 times) amplitude than that for Δi_R . It is direct experimental evidence of a substantial decrease in the concentration overpotential (η_c) that overcomes the ohmic contribution to give an increase in the total current. Such an increase agrees with the prediction by Dukovic and Tobias and by Vogt in the previous section.

Ohmic Resistance. Ohmic resistance can be further caused by the dispersion of bubbles in the electrolyte. There are numerous theoretical equations that describe the electrical conductivity of electrolyte solution ($\kappa_{\text{bubble, sol}}$) filled with gas bubbles as a function of the volume fraction of gas bubbles (p).^{91,92} Below are the four most popular equations separately derived by Maxwell,⁹³ Jeffery⁹⁴ and Prager,⁹⁵ Meredith and Tobias,⁹⁶ and Bruggeman⁹⁷

$$\frac{\kappa_{\text{bubble, sol}}}{\kappa_{\text{sol}}} = \begin{cases} \frac{1-p}{1+\frac{p}{2}} & \text{Maxwell} \\ (1-1.5p+xp^2) & \text{Jeffery \& Prager} \\ \frac{8(2-p)(1-p)}{(4+p)(4-p)} & \text{Meredith \& Tobias} \\ (1-p)^{1.5} & \text{Bruggeman} \end{cases} \quad (10)$$

where κ_{sol} is the electrolyte conductivity in the absence of gas bubbles. The corresponding models used in their derivations are schematically depicted in Figure 8A. Maxwell's model is

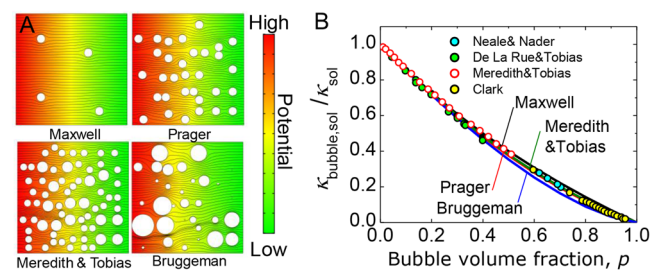


Figure 8. (A) Illustration of the theoretical models for predicting the conductivity of dispersions in a solution used by Maxwell, Prager, Meredith and Tobias, and Bruggeman. (B) Comparison between experimental data and theoretical predictions of solution conductivity as a function of the bubble volume fraction.

applicable to a special case where the electrolyte is randomly filled with spherical gas bubbles having the same radii.⁹³ Jeffery⁹⁴ and Prager⁹⁵ modified Maxwell's equation after taking the interactions between bubbles into account. Their results agree with Maxwell's result at low gas volume fraction and significantly improve on it over medium and high volume fractions. For the mixtures of bubbles of various sizes, there are two available models. Meredith and Tobias⁹⁶ devised an approach called the distribution model by considering only two different sizes in equal volume fractions. The other one was developed by Bruggeman⁹⁷ and considers a pseudocontinuous

distribution of sizes by accumulating the contributions of a range of bubble sizes.

Experimental validation of the above expressions was carried out using a conductivity cell filled with materials of well-defined shape such as glass beads,^{89,98,99} emulsions,⁹⁶ and foams.¹⁰⁰ Figure 8B shows the comparison between experimental data and the theoretical predictions by various models.^{96,98–100} Overall, the deviations between these equations are less than 10%, suggesting that any of the equations can be used to estimate the bubble-induced electrolyte ohmic resistance. We point out that the theoretical and experimental studies discussed above are based on largely simplified static models and the assumption of a uniform distribution of bubbles in electrochemical cells, both of which can substantially deviate from practical applications. There are numerous studies on the bubble-induced ohmic resistance in specific operating systems.^{101–113} For example, Vogt¹⁰⁵ built a hydrodynamic model for the ohmic resistance of cells under the assumption that the dispersion of gas bubbles in an electrolyte can be treated as two parts: a stagnant boundary at the electrodes being enriched in gas and flowing bulk in the center region. In following years, he continued to modify this model by considering that only a fraction of the dissolved gas turns into gas bubbles¹⁰³ and by treating the flow rates of gas bubbles and electrolyte solution separately.¹⁰⁴ Kreysa and Kuhn¹⁰⁹ derived new equations for calculating the gas bubble fraction as a function of the gas bubble velocity by introducing a coalescence barrier model, where gas bubbles in a swarm are separated from each other by a minimum distance due to electrostatic repulsion. Experimentally, Baker¹⁰¹ measured the gas volume fraction as a function of vertical distance from the bottom of the cell and the corresponding current density. Bongenaar-Schlenter et al.¹⁰² measured the bubble distribution as a function of the distance to the electrode surface during alkaline water electrolysis, taking advantage of the light-screening property of gas bubbles. Janssen and co-workers focused on the experimental investigation of the ohmic resistance in operating alkaline water electrolyzers.^{106,107,114}

Mass Transfer. Several mass transfer processes are simultaneously occurring at gas-evolving electrodes, including mass transfer of the reactants from the bulk electrolyte to the electrode surface, and the products back to bulk electrolyte or to the gas–liquid interface. Gas bubbles influence these processes via various mechanisms. One mechanism is that the presence of bubbles affects the mass transfer of dissolved gas by imposing a concentration boundary condition at the gas bubble/electrolyte interface as discussed in Figure 5. Another mechanism is that evolved bubbles can enhance heat or mass transport by convection, as the growing and detaching gas bubbles mix electrolyte near the electrode with that in the bulk. Because the improved heat transfer by evolved bubbles usually has an insignificant influence on the performance of a gas evolution system, rather little has been published on the heat transfer at gas-evolving electrodes.^{115–117} Therefore, we will focus our discussion on mass transfer in this section. If the reaction rate is controlled by mass transfer, then bubbling accelerates the transport of reaction species to the electrode. Figure 9 shows the experimental evidence of this enhancement effect. In this experiment, Fouad and Sedahmed¹¹⁸ measured the mass transfer coefficients of two indicator ions (k) during water electrolysis [$K_3Fe(CN)_6$ and $K_4Fe(CN)_6$] and related k to the volumetric flux of gas evolved at the electrode (V). The mass transfer rates of $K_3Fe(CN)_6$ and $K_4Fe(CN)_6$ are

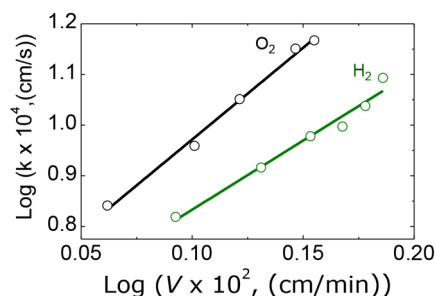


Figure 9. Effect of the volumetric flux (V) of O_2 and H_2 evolved at the electrodes on the mass transfer coefficient (k) of two indicator species, $K_3Fe(CN)_6$ and $K_4Fe(CN)_6$, during water electrolysis. The indicator species were either oxidized or reduced at the electrodes in the presence of bubble evolution. k was obtained by determining the change in indicator ion concentrations in the electrolyte during water electrolysis. Reproduced with permission from ref 118, copyright 1973 by Elsevier.

significantly boosted as the gas discharge rate increases. The most interesting finding is the linear relation between k and V in the log–log coordinates. Similar linear relations have been widely reported in many other experimental investigations.^{83,119–128} Vogt unified these results using an empirical correlation¹²⁹

$$k = \text{const}(V)^m \quad (11)$$

where m ranges from ~ 0.2 to 0.7 depending on the reaction conditions.

A few theoretical models have been constructed to explain and correlate this experimental observation. Figure 10 shows

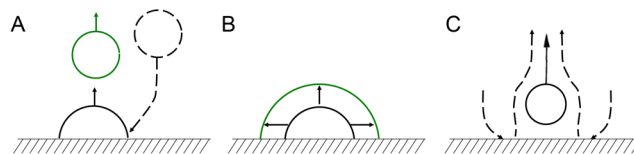


Figure 10. Schematic representation of the three classical models for mass transfer at gas-evolving electrodes. (A–C) Penetration model, microconvection model, and hydrodynamic model, respectively.

three classical models for mass transfer at gas-evolving electrodes according to Vogt¹²⁹ and Sides.⁹¹ The first one is the penetration model developed by Ibl and co-workers.¹³⁰ In this model, the diffusion of the reactant from fresh electrolyte, brought to the surface after a bubble detaches, is the mechanism for mass transfer enhancement. The periodic renewal of electrolyte solution near the electrode slows down the expansion of the diffusion layer, which helps to sustain a high flux of reactant. Derived from the Cottrell equation, they obtained an analytical expression of the mass transfer coefficient in the form of eq 11 with $m = 0.5$.

The second model is the microconvection model proposed by Stephan and Vogt.¹³¹ This model differs from the penetration model mainly because it considers only convective mass transfer. As an adhering bubble grows, it pushes away the liquid in its vicinity. Once the bubble becomes sufficiently large, it detaches from the surface and a new bubble forms and grows at the same site, resulting in a periodic disturbance of the diffusion layer and thus an enhancement of mass transfer. Adapted from the mass transfer theory for laminar flow over a

plane, the local and temporal mass transfer coefficient k_x is given by

$$k_x = \text{const} \left(\frac{Dv_x}{x} \right)^{0.5} \quad (12)$$

where v_x is the fluidic velocity induced by bubble expansion and x is the distance from the bubble. The overall mass transfer coefficient, k , is the mean value of k_x in the residence time of the bubble and the area pertinent to each adhering bubble. After relating v_x to V , k can also be approximately expressed as eq 11 with the exponent $m = 0.5$. More recently, Vogt and Stephan¹³² revisited their theory and proposed a unified local microprocess model by considering microconvection, penetration, and wake flow transport altogether, which also gives an m value of ~ 0.5 . The difference between this new model and previous ones, however, is the significant dependence of the prefactor in eq 11 on the bubble surface coverage and electrolyte flow rate.

The third model is the hydrodynamic model first proposed by Janssen and Hoogland.¹²² In this model, the free-convective flow of electrolyte, caused by the rising bubble swarm, is the reason for improved mass transfer. The expression of mass transfer coefficient is derived from the mass transfer equations for natural turbulent convection at a plane wall is

$$k = \text{const} (Z_d g V / \nu D \nu_t)^{1/3} \quad (13)$$

where ν_t is the terminal velocity of a bubble, ν is the kinematic viscosity of the fluid, D is the diffusion coefficient, and Z_d is the drag coefficient on a bubble. With the recent development of powerful computational modeling tools, significant advancements have been made in the understanding of bubble–electrolyte two-phase flow hydrodynamics, which have been reviewed by the Lopicque group¹³³ and the Alshawabkeh group.¹³⁴

Besides the three classical models, new theories have also been proposed with recent experimental findings. For example, Eckert and co-workers^{135,136} found much stronger convection at the foot of a bubble than that at the top (Figure 11) using particle tracking velocimetry. More interestingly, the maximum in the velocity was at the interface rather than in the solution, thereby differing from that of buoyancy-driven flow. Therefore,

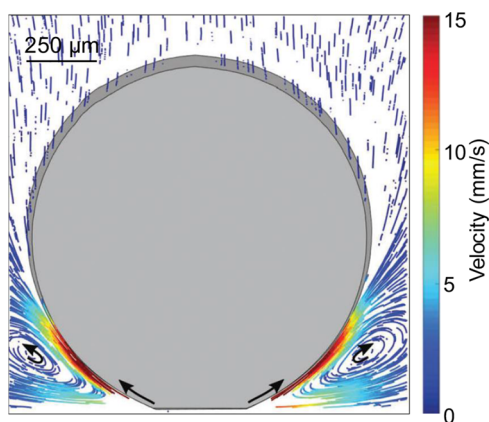


Figure 11. Flow velocity around an electrogenerated H_2 bubble measured by particle tracking velocimetry indicating the existence of Marangoni convection near this electrogenerated bubble. Reproduced with permission from ref 135, copyright 2018 by the Royal Society of Chemistry.

they proposed that Marangoni convection existed at electro-generated bubbles, which might be caused by the inhomogeneous hydrogen concentration or ohmic heating, thus resulting in a gradient of the surface tension along the bubble interface.

Catalyst Stability. How to overcome long-term catalyst degradation and sustain high activity is a grand challenge in the field of electrocatalysis.^{137,138} For example, iridium-based mixed oxides were found to be highly active OER catalysts, but these structures have been shown to degrade significantly in acidic electrolyte during OER.¹³⁹ The major degradation process of the mixed oxides has been attributed to the dissolution of non-noble alkali or rare-earth element components in acidic electrolytes. The contribution of evolved bubbles to the degradation of electrocatalytic materials was, however, not paid much attention, even though gas bubbles have long been suspected to cause mechanical damage to their surrounding materials.^{70,140,141} One reason is the challenge in obtaining direct evidence of bubble-caused catalyst degradation. Most recently, Shao-Horn and co-workers¹⁶ found direct evidence of bubble-induced structural changes of a catalyst during oxygen evolution using in situ TEM. They observed that the formation and collapse of gaseous bubbles within perovskite oxide particles caused the structural oscillations of the catalyst (Figure 12). The structural oscillation was explained by the uptake of water into the perovskite oxide and the e-beam-induced O_2 evolution inside the oxide.

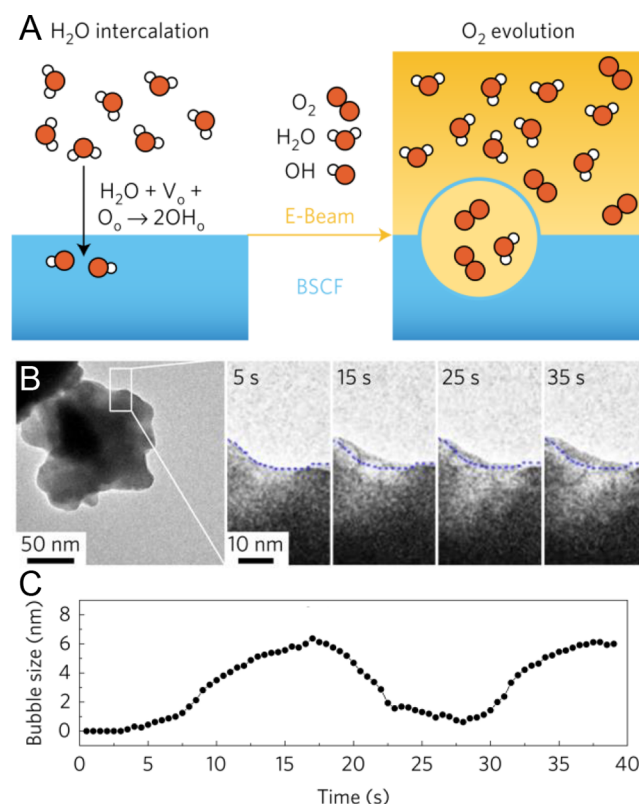


Figure 12. (A) Schematic of water incorporation accompanied by water splitting within $\text{Ba}_{0.5}\text{Sr}_{0.5}\text{Co}_{0.8}\text{Fe}_{0.2}\text{O}_{3-\delta}$ (BSCF) perovskite oxide particles, which leads to structural oscillations observed on BSCF in H_2O vapor under e-beam irradiation. (B) Images of the structural oscillations of BSCF. The blue dashed lines are guides to help in the comparison of the motion of the particle edges. (C) Measured bubble size vs time. Reproduced with permission from ref 16, copyright 2017 by Springer Nature.

Although the experimental conditions used in their study (H_2O vapor plus electron beam irradiation) are not identical to the typical OER conditions, the result is still suggestive of similar bubble-induced structural changes during OER.

■ CONTROLLED BUBBLE BEHAVIOR FOR ELECTROCATALYSIS

In the previous two sections, we have reviewed the formation of bubbles as well as their impacts on a gas-evolving system. These fundamental studies are critical to developing new bubble-based strategies to achieve improved functionality and performance for gas-evolving electrocatalysis, which will be discussed in this section.

Bubble Generation Control. During gas evolution reactions, gas bubbles nucleate at the reaction interface where the electrolyte solution is supersaturated with evolved gas. White and co-workers have investigated the formation of single bubbles at the surface of nanoelectrodes. The bubbles were generated with confined dissolved-gas supersaturations at the reaction interface. For instance, the critical concentrations of dissolved gas at the reaction interface for H_2 , N_2 , and O_2 bubble generation were demonstrated to be 0.23, 0.09, and 0.14 M, respectively.¹¹ As introduced in previous section, such supersaturation of evolved gas causes a concentration overpotential at the reaction interface.

Inspired by this overpotential mechanism, our group recently developed a facile strategy for highly efficient HER through tailoring the dissolved gas concentration at the reaction interface via potassium perfluorooctanesulfonate (PFOS) modulation.¹⁴² The addition of PFOS facilitates bubble generation due to its high surface activity, which lowers the bubble nucleation energy. As the applied current for H_2 evolution was stepped from 10^{-5} to 5×10^{-4} A, H_2 bubbles started forming at a much lower current of 5×10^{-5} A for PFOS-Pt than for pure Pt (Figure 13A). The facilitated bubble

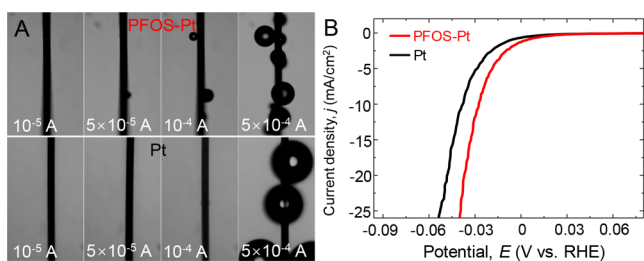


Figure 13. (A) Photographs showing bubble generation behaviors for PFOS-Pt (top) and pure Pt (bottom). The black bands are the 50- μm -thick Pt wire electrodes. (B) *iR*-corrected polarization curves for PFOS-Pt and pure Pt. Reproduced with permission from ref 142, copyright 2019 by the Royal Society of Chemistry.

formation caused a decrease in the interfacial concentration of dissolved H_2 following the possible mechanism discussed in Figure 5. In addition, the blockage of surface sites by PFOS surfactant was demonstrated to be inhibited by the desorption of PFOS during the reaction, ensuring the sufficient exposure of active sites for HER. Taken together, the lowered interfacial concentration of dissolved H_2 and the sufficient exposure of active sites result in the remarkable electrocatalytic HER performance of PFOS-Pt (Figure 13B). PFOS-Pt had a much lower overpotential of 27 mV compared to 38 mV for pristine Pt at a cathodic current density of 10 mA cm^{-2} . This tuning strategy provides a promising avenue for managing the bubble

generation behaviors at the reaction interface for efficient gas-evolving electrocatalysis.

Bubble Release Management. Adhering bubbles to the electrode surface hinders the diffusion of electrolyte, reduces the surface area, and increases the ohmic drop, resulting in a low reaction efficiency.^{143–145} How to effectively remove bubbles from the electrode surface represents another critical issue for high-performance electrocatalysis. Ultrasonic and ultragravity treatments are possible means of promoting bubble detachment, but their industrial applications are limited because static working conditions are preferred for electrochemical cells.^{146–148} As such, it is meaningful to develop alternative strategies to manage the bubbles release during gas evolution reactions.

According to the theory of bubble detachment previously discussed, the detachment of a bubble is governed by the force balance between buoyancy (F_b) and the adhesion force (F_a) (Figure 14A). To promote bubble release, one popular strategy

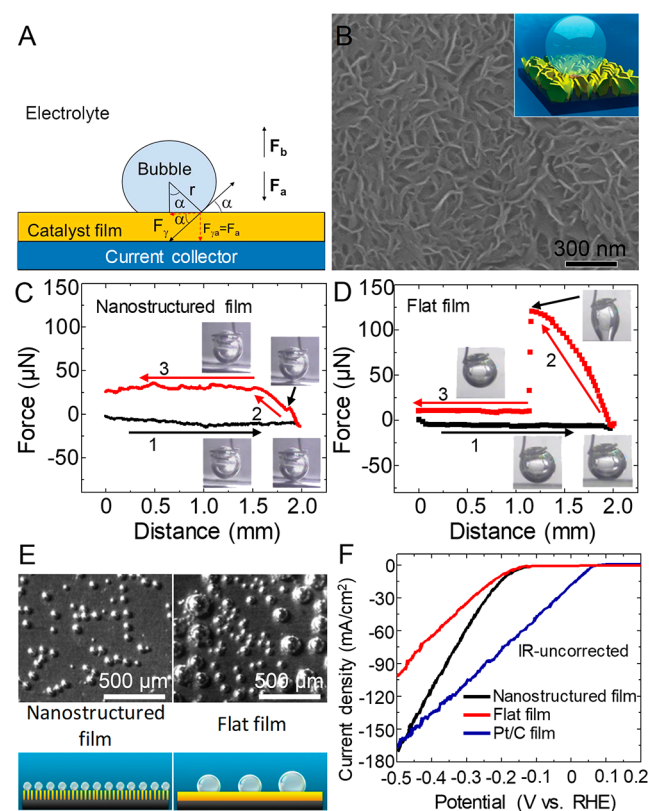


Figure 14. (A) Force analysis of an as-formed gas bubble on the surface of a catalyst film in an aqueous electrolyte. (B) Top-view SEM image of nanostructured MoS_2 films. The inset shows the adhesion behavior of a gas bubble on a nanostructured film. (C, D) Measured adhesive forces of gas bubbles on nanostructured and flat films. (E) Images showing the difference in bubble generation behavior on nanostructured and flat films. (F) Polarization curves of MoS_2 and Pt/C catalysts. Reproduced with permission from ref 149, copyright 2014 by John Wiley & Sons, Inc.

is to fabricate “superaerophobic” electrodes with decreased adhesion force.^{149,150} By tailoring the micro/nanoarchitecture of an electrode, the electrode/gas bubble/electrolyte interface can become discontinuous, resulting in a minimal true contact area and low adhesion force between the as-formed gas bubbles with the superaerophobic electrode surface. Sun and

co-workers¹⁴⁹ demonstrated this concept using a nanostructured MoS₂ thin film (Figure 14B) as the electrode for HER. The nanostructured MoS₂ showed an adhesive force of $11 \pm 2 \mu\text{N}$ (Figure 14C), $\sim 10\%$ of $125 \pm 6 \mu\text{N}$ for a flat MoS₂ film electrode (Figure 14D). The adhesive forces were measured using a microelectromechanical balance system. As shown in Figure 14 C,D, the electrode surfaces were first brought into contact with a gas bubble (step 1). When the surfaces left the gas bubble after contact, the balance force increased gradually and reached a critical force at the end of step 2. Finally, the surfaces broke away from the gas bubble in step 3. The critical force was regarded as the adhesive force between the electrode interfaces and the gas bubble. The largely decreased adhesive force for the nanostructured MoS₂ film led to small bubble sizes and reduced bubble coverage (Figure 14E), thus improving the HER activity (Figure 14F). The same group has also reported a similar enhancement effect using a nanostructured NiMo film for HER,¹⁵¹ NiFe-LDH mesoporous films for OER,¹⁵¹ a RuO₂@TiO₂ nanosheet array electrode for CER,¹⁵² and a Cu nanoporous film, Ni nanosheet array, and Ni nanoflower electrode for HzOR.^{153–155} Besides the Sun group, several other groups have also explored the use of superaerophobic electrodes for gas evolution reactions and found similar activity improvement.^{156–161}

Furthermore, the electrode stability was also found to be associated with the release behavior of gas bubbles during gas-evolving electrocatalysis. For instance, Li et al. found¹⁶² that the pine-shaped Pt nanoarray electrode showed superior stability for HER as compared to a flat Pt electrode. The HER current of the Pt nanoarray electrode was much more stable than that of a flat electrode during a 36 h stability test. In addition, the SEM images showed the bubble-induced scratches and morphology changes on the flat Pt electrode after the stability test. In contrast, the Pt nanoarray electrode showed little morphology change. The improved stability for the pine-shaped Pt nanoarray electrode was attributed to the reduced adhesion force between the evolved bubbles and the superaerophobic surface. The enhanced stability has also been demonstrated on CoS₂ with different structures.¹⁴⁰ Compared to flat CoS₂ films, CoS₂ nanowire (NW) and microwire (MW) arrays were more efficient in removing the bubbles and preventing them from damaging the electrodes (Figure 15A,B). After a 41 h stability test at 10 mA cm^{-2} , the HER overpotential for the CoS₂ microwire array increased only by about 20 mV (Figure 15C). In comparison, the flat CoS₂ film showed a dramatic increase in overpotential by $>200 \text{ mV}$ after 3 h of the stability test.

More recently, Sinton and co-workers¹⁶³ demonstrated another interesting application of bubble release in electrocatalysis. They showed that the morphology of gold nanoneedle electrodes enhanced long-range CO₂ transport via their influence on bubble release during CO₂ electroreduction. The CO₂ reduction rate for CO production increased by 4-fold in the diffusion-limited region compared to that for a nanoparticle-based catalyst, leading to improved product selectivity toward CO₂ reduction.

Bubble-Assisted Electrocatalyst Fabrication. Bubbles play another significant role in electrocatalysis via assisting the construction of electrode structures. The fabrication of porous electrocatalytic materials has been demonstrated using bubble-templated electrodeposition. Liu et al.¹⁶⁴ reported the construction of Cu and Sn porous foams using this method. The generated hydrogen bubbles create a path with a

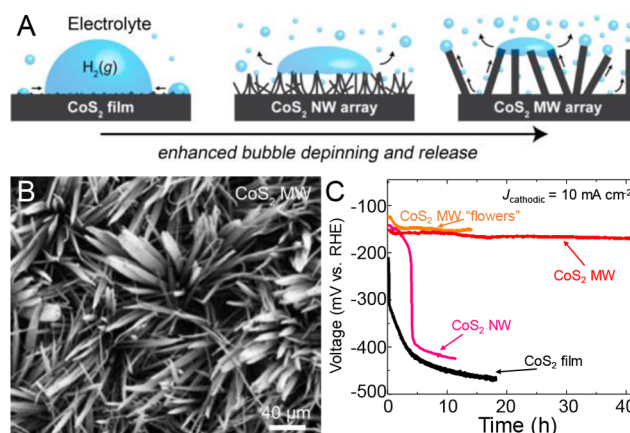


Figure 15. (A) Schematic depictions of CoS₂ nanowire (NW) and microwire (MW) arrays effectively wicking the evolved bubbles and maintaining the solid–liquid interface. (B) SEM image of CoS₂ MWs. (C) Long-term stability of different CoS₂ structures for HER. Reproduced from ref 140, copyright 2014 by the American Chemical Society.

decreased amount and disrupted diffusion of metal ions, thereby leading to the electrodeposition between bubbles and the porous structures. Because of bubble coalescence, the pore size in the electrodeposited foams increased with the distance away from the substrate. By adding acetic acid, bubble coalescence could be suppressed, leading to reduced pore sizes and an increased pore density in the deposited foams.¹⁶⁵ Xia et al.¹⁶⁶ found that the pore sizes in Cu films could also be controlled by electrolyte concentration, applied currents, and surfactant concentration. With a low Cu ion concentration and a large current density, hydrogen evolution was accelerated, producing large convection in electrolytes and small bubbles. The presence of surfactants inhibited the bubble coalescence and resulted in a well-dispersed bubble template. Porous Au films were also prepared by the galvanic exchange reaction between bubble-assisted deposited Cu films and Au salts.¹⁶⁷ Similar bubble-templated electrodeposition has also been demonstrated to fabricate other porous metals (Co, Ag, Ni, Pd, Pt, Bi, and Ru),^{168–173} alloys (NiAg, NiCo, NiSn, NiCoFe, CuNi, CuPd, CuAu, CuPt, AuPt, PdNi, and PtPd),^{174–184} oxides (PbO₂ and MnO₂),^{185,186} and graphene-based materials.¹⁸⁷

Owing to the porous structure, electrode materials prepared by bubble-templated electrodeposition often exhibit improved electrocatalytic performance. For example, Broekmann and co-workers¹⁸⁸ developed a porous Ag foam electrode for CO₂ electroreduction using a citrate-modified electrodeposition approach with bubble assistance (Figure 16). The citrate additives reduced the interfacial tension and thus led to the decreased bubble size during foam deposition. The obtained Ag-foam catalyst has a particular mesoporosity with pore sidewalls that are composed of highly anisotropic, needle-shaped Ag features having dimensions in the nanometer range (Figure 16B). This unique porous structure of Ag foam exhibited a higher CO adsorption energy in comparison to Ag foil, resulting in a high activity for CO production at low and moderate overpotentials and the capability for hydrocarbon production at high overpotentials. In another example, Kwon et al.¹⁸⁹ synthesized a porous Co–P foam electrode by bubble-templated electrodeposition on a Cu substrate (Figure 17). As shown in Figure 17C,D, the porous Co–P foam exhibited a

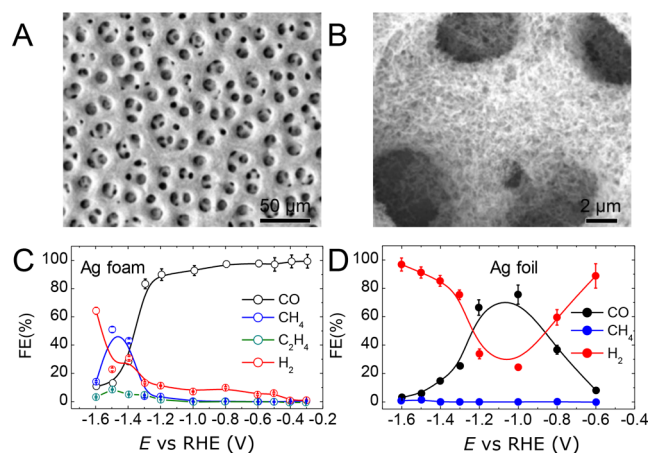


Figure 16. (A and B) Top-down SEM images showing the macroporosity of an Ag foam prepared by bubble-templated electrodeposition. (C and D) Potential-dependent product distributions of the electrochemical CO_2 reduction on Ag foam and Ag foil. Reproduced from ref 188, copyright 2018 by the American Chemical Society.

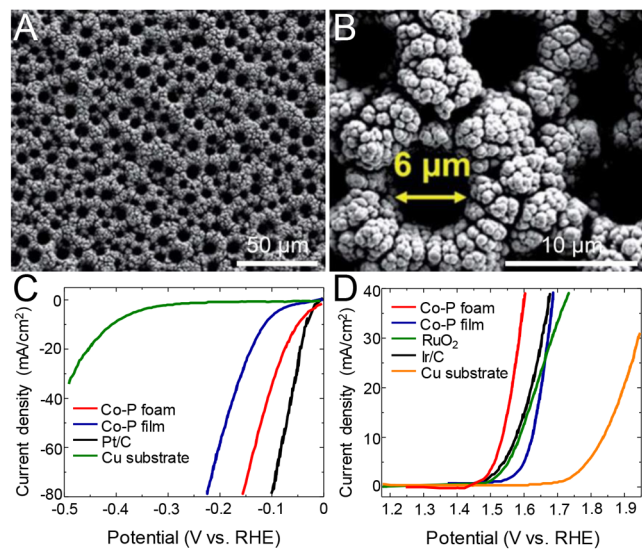


Figure 17. (A and B) SEM images of an electrodeposited Co–P foam on a Cu substrate with bubble assistance at different magnifications. (C) HER and (D) OER activities of catalysts. Reproduced with permission from ref 189, copyright 2016 by the Royal Society of Chemistry.

much lower overpotential at 10 mA cm^{-2} for both OER and HER than did the Co–P film electrode. The excellent performance of the Co–P foam as a HER and OER catalyst was partially attributed to the porous foam structure providing a large electrochemically active surface area, which was calculated to be as 2.4 times higher than that of a typical Co–P film. Similarly, Chen et al.¹⁹⁰ developed NiCuP foams on stainless steel foils via electrodeposition using hydrogen bubbles as the template, followed by phosphidization. The synthesized NiCuP foams showed improved HER and OER activities that were better than those for commercial Pt/C and IrO_2 catalysts, respectively.

OUTLOOK

In the previous sections, we have reviewed the classical theories as well as recent advancements in the field of gas bubbles in electrochemical gas evolution reactions. Although progress has been made in this field, we believe that there are two important subfields that need more research: bubble behavior at the nanoscale and bubbles in selective electrocatalysis.

Limited by the analytical tools and methods at the time, much of the previous work on electrogenerated bubbles was focused on bubble behavior on the micrometer scale and above. How bubbles behave during gas evolution reactions on the nanoscale remains mostly unknown. As more evidence is delivering the message that the nanostructure of an electrocatalyst determines the overall activity, it also urges us to answer a similar question: how do the bubble behaviors at the nanoscale affect the electrocatalytic activity?

To answer this question, several analytical methods are being developed for the study of nanosized bubbles or nanobubbles, including atomic force microscopy,¹⁷ single-molecule fluorescence microscopy,^{18,19} dark-field microscopy,^{20,21,191} nanoelectrochemistry,¹⁴ and in situ TEM.¹⁶ With the help of these tools, one will be able to observe bubble behavior on the nanoscale with an unprecedentedly high time and spatial resolution. The new knowledge will lead to new understandings of the activity of electrocatalysts, new methods to identify the active sites for establishing the structure–activity relationship, and new strategies to improve the activities by controlling bubble behavior. For example, our recent work³⁶ has shown that Pt and Au nanodomains exhibit similar bubble nucleation conditions even though their HER activities dramatically differ. Our finding provides valuable fundamental insight into the relationship between the bubble formation potential and the local HER activity. It could guide the development of a bubble-based method that uses the bubble formation potential as the criterion for rapidly and conveniently evaluating the HER activity distribution on a catalytic surface or in an ensemble of catalytic nanoparticles.

In another example, AFM studies have revealed the exotic stability and shape of surface nanobubbles. The classical theory predicts that a bubble with a 100 nm radius should dissolve in microseconds due to the massive Laplace pressure inside these nanoscopic objects.^{192,193} However, they were found to live for hours under ambient conditions.¹⁹⁴ Also, surface bubbles were found to be spherical caps, quasi-2D so-called micropancakes, or a combination of the two.¹⁹⁵ The gas micropancakes are only a few nanometers thick but spread up to several micrometers wide. The cross-sectional profile of micropancakes is flat on the top with the curvature at the boundary. Gas micropancakes have been observed only on crystalline substrates in water including HOPG, talc, and MoS_2 .^{196,197} Furthermore, a superresolution fluorescence microscopic study by Zhang and co-workers¹⁸ has shown that the spatial distribution of surface nanobubbles on an oxide-supported metal nanoparticle catalyst during HER is a function of electrode potential rather than always being at the most active nanoparticle sites. All of the above behaviors of surface nanobubbles might significantly affect the surface blockage.

Besides bubble behavior at the nanoscale, the influence of gas bubbles on selective electrocatalysis is underexplored as well. Because the earlier bubble-related work was mainly motivated by the development of water electrolyzers, the

research focus was on the efficiency of HER and OER. As society now seeks environmentally compatible processes to reduce energy consumption and fossil fuel usage and to replace toxic or dangerous oxidizing or reducing reagents, electrosynthesis is emerging as the “chosen one” because of its potential to be green and its ability to achieve certain transformations that are difficult by conventional chemical approaches.^{198–202} However, because of the narrow electrochemical stability window of water, electrosynthesis can often experience interference from side reactions of water: the HER and OER, leading to low energy efficiency. For example, the conversion of CO₂ to hydrocarbons is always accompanied by HER when performed in aqueous solutions.²⁰³ Likewise, HER seriously harms the energy efficiency of electrochemical N₂ reduction.^{198,204} Being the direct products from the side reactions of water, H₂ and O₂ gas bubbles are undoubtedly worthy of careful investigations: how and where do the gas bubbles start forming? How do we suppress their generation? During selective electrocatalysis, gas bubbles are generated not only by the HER and OER but also by the non-water-splitting electrocatalytic reactions of interest. For example, CO₂ can be electrochemically reduced to various gas products including CH₄, CO, C₂H₄, and C₃H₈. Successful identification of the gas bubbles on a CO₂RR catalyst surface will potentially lead to new findings regarding the active structures with desired product selectivity.

AUTHOR INFORMATION

Corresponding Author

*E-mail: long.luo@wayne.edu

ORCID

Hang Ren: 0000-0002-9480-8881

Long Luo: 0000-0001-5771-6892

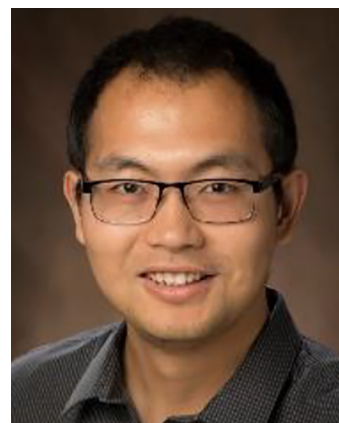
Notes

The authors declare no competing financial interest.

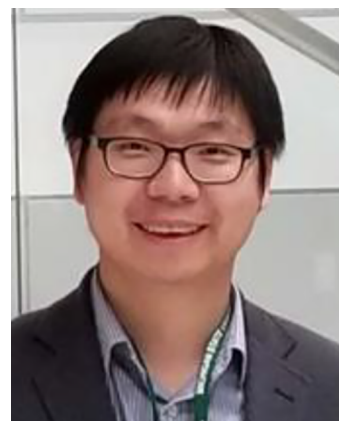
Biographies



Xu Zhao received his B.S. from Zhengzhou University in 2013 and Ph.D. (with Prof. Jie Zeng) from the University of Science and Technology of China in 2018. He is currently a postdoctoral fellow in Prof. Long Luo's group at Wayne State University. His current research interests include the atomic-level design of nanomaterials and control of interfacial mass transfer for electrocatalysis.



Hang Ren received his B.S. from Sun Yat-sen University in 2011 and Ph.D. from the University of Michigan in 2016. After 2 years of postdoctoral work at the University of Utah, he is now an assistant professor in the Department of Chemistry and Biochemistry at Miami University. His current research interest is single entity electrochemistry for energy and biomedical applications.



Long Luo is currently an assistant professor in the Department of Chemistry at Wayne State University. He received his B.S. (2009) in applied chemistry from Beijing University of Aeronautics and Astronautics and his Ph.D. (2014) in chemistry from the University of Utah. Before joining Wayne State University in 2017, he worked as a postdoctoral fellow in the Department of Chemistry at the University of Texas at Austin. His current research interests include electrogenerated bubbles, electrochemical synthesis, and electrokinetic phenomena.

ACKNOWLEDGMENTS

L.L. and X.Z. acknowledge start-up funds and the Ebbing Faculty Development Award from Wayne State University. H.R. acknowledges generous start-up funds provided by Miami University.

REFERENCES

- (1) Voiry, D.; Shin, H. S.; Loh, K. P.; Chhowalla, M. Low-Dimensional Catalysts for Hydrogen Evolution and CO₂ Reduction. *Nat. Rev. Chem.* **2018**, *2*, 0105.
- (2) Zhao, X.; Xing, Y.; Zhao, L.; Lu, S.; Ahmad, F.; Zeng, J. Phosphorus-Modulated Cobalt Selenides Enable Engineered Reconstruction of Active Layers for Efficient Oxygen Evolution. *J. Catal.* **2018**, *368*, 155–162.
- (3) Zhao, X.; Li, X.; Yan, Y.; Xing, Y.; Lu, S.; Zhao, L.; Zhou, S.; Peng, Z.; Zeng, J. Electrical and Structural Engineering of Cobalt Selenide Nanosheets by Mn Modulation for Efficient Oxygen Evolution. *Appl. Catal., B* **2018**, *236*, 569–575.

- (4) Grimaud, A.; Diaz-Morales, O.; Han, B.; Hong, W. T.; Lee, Y.-L.; Giordano, L.; Stoerzinger, K. A.; Koper, M. T.; Shao-Horn, Y. Activating Lattice Oxygen Redox Reactions in Metal Oxides to Catalyze Oxygen Evolution. *Nat. Chem.* **2017**, *9*, 457–465.
- (5) Zhang, J. Y.; Wang, H.; Tian, Y.; Yan, Y.; Xue, Q.; He, T.; Liu, H.; Wang, C.; Chen, Y.; Xia, B. Y. Anodic Hydrazine Oxidation Assists Energy Efficient Hydrogen Evolution over a Bifunctional Cobalt Perselenide Nanosheet Electrode. *Angew. Chem., Int. Ed.* **2018**, *57*, 7649–7653.
- (6) Zhao, X.; Zhang, H.; Yan, Y.; Cao, J.; Li, X.; Zhou, S.; Peng, Z.; Zeng, J. Engineering the Electrical Conductivity of Lamellar Silver Doped Cobalt (II) Selenide Nanobelts for Enhanced Oxygen Evolution. *Angew. Chem., Int. Ed.* **2017**, *56*, 328–332.
- (7) Yang, J.; Cooper, J. K.; Toma, F. M.; Walczak, K. A.; Favaro, M.; Beeman, J. W.; Hess, L. H.; Wang, C.; Zhu, C.; Gul, S.; et al. A Multifunctional Biphasic Water Splitting Catalyst Tailored for Integration with High-Performance Semiconductor Photoanodes. *Nat. Mater.* **2017**, *16*, 335–341.
- (8) Lu, Q.; Rosen, J.; Zhou, Y.; Hutchings, G. S.; Kimmel, Y. C.; Chen, J. G.; Jiao, F. A Selective and Efficient Electrocatalyst for Carbon Dioxide Reduction. *Nat. Commun.* **2014**, *5*, 3242.
- (9) Guo, C.; Zheng, Y.; Ran, J.; Xie, F.; Jaroniec, M.; Qiao, S. Z. Engineering High Energy Interfacial Structures for High Performance Oxygen Involving Electrocatalysis. *Angew. Chem., Int. Ed.* **2017**, *56*, 8539–8543.
- (10) Karlsson, R. K.; Cornell, A. Selectivity between Oxygen and Chlorine Evolution in the Chlor-Alkali and Chlorate Processes. *Chem. Rev.* **2016**, *116*, 2982–3028.
- (11) German, S. R.; Edwards, M. A.; Chen, Q.; Liu, Y.; Luo, L.; White, H. S. Electrochemistry of Single Nanobubbles. Estimating the Critical Size of Bubble-Forming Nuclei for Gas-Evolving Electrode Reactions. *Faraday Discuss.* **2016**, *193*, 223–240.
- (12) Zhang, X. H. Quartz Crystal Microbalance Study of the Interfacial Nanobubbles. *Phys. Chem. Chem. Phys.* **2008**, *10*, 6842–6848.
- (13) Zhang, X. H.; Quinn, A.; Ducker, W. A. Nanobubbles at the Interface between Water and a Hydrophobic Solid. *Langmuir* **2008**, *24*, 4756–4764.
- (14) Luo, L.; White, H. S. Electrogenation of Single Nanobubbles at Sub-50-nm-Radius Platinum Nanodisk Electrodes. *Langmuir* **2013**, *29*, 11169–11175.
- (15) Lohse, D. Bubble Puzzles: From Fundamentals to Applications. *Phys. Rev. Fluids* **2018**, *3*, 110504.
- (16) Han, B.; Stoerzinger, K. A.; Tileli, V.; Gamalski, A. D.; Stach, E. A.; Shao-Horn, Y. Nanoscale Structural Oscillations in Perovskite Oxides Induced by Oxygen Evolution. *Nat. Mater.* **2017**, *16*, 121–126.
- (17) Lou, S.-T.; Ouyang, Z.-Q.; Zhang, Y.; Li, X.-J.; Hu, J.; Li, M.-Q.; Yang, F.-J. Nanobubbles on Solid Surface Imaged by Atomic Force Microscopy. *J. Vac. Sci. Technol., B: Microelectron. Process. Phenom.* **2000**, *18*, 2573–2575.
- (18) Hao, R.; Fan, Y.; Howard, M. D.; Vaughan, J. C.; Zhang, B. Imaging Nanobubble Nucleation and Hydrogen Spillover during Electrocatalytic Water Splitting. *Proc. Natl. Acad. Sci. U. S. A.* **2018**, *115*, 5878–5883.
- (19) Su, H.; Fang, Y.; Chen, F.; Wang, W. Monitoring the Dynamic Photocatalytic Activity of Single CdS Nanoparticles by Lighting Up H₂ Nanobubbles with Fluorescent Dyes. *Chem. Sci.* **2018**, *9*, 1448–1453.
- (20) Ma, Y.; Highsmith, A. L.; Hill, C. M.; Pan, S. Dark-Field Scattering Spectroelectrochemistry Analysis of Hydrazine Oxidation at Au Nanoparticle-Modified Transparent Electrodes. *J. Phys. Chem. C* **2018**, *122*, 18603–18614.
- (21) Zhang, T.; Li, S.; Du, Y.; He, T.; Shen, Y.; Bai, C.; Huang, Y.; Zhou, X. Revealing the Activity Distribution of a Single Nanocatalyst by Locating Single Nanobubbles with Super-Resolution Microscopy. *J. Phys. Chem. Lett.* **2018**, *9*, 5630–5635.
- (22) Zhang, X.; Winnik, F. M. Preface to the Nanobubbles Special Issue. *Langmuir* **2016**, *32*, 11071–11071.
- (23) Ford, I. Nucleation Theorems, the Statistical Mechanics of Molecular Clusters, and a Revision of Classical Nucleation Theory. *Phys. Rev. E: Stat. Phys., Plasmas, Fluids, Relat. Interdiscip. Top.* **1997**, *56*, S615–S629.
- (24) Kalikmanov, V. I. Classical Nucleation Theory. *Nucleation Theory*; Springer: 2013; pp 17–41.
- (25) German, S. R.; Edwards, M. A.; Ren, H.; White, H. S. Critical Nuclei Size, Rate, and Activation Energy of H₂ Gas Nucleation. *J. Am. Chem. Soc.* **2018**, *140*, 4047–4053.
- (26) Bon, C. K. *Supersaturation at Gas-Evolving Electrodes*; University of California Berkeley: Berkeley, CA, 1970.
- (27) Shibata, S. The Concentration of Molecular Hydrogen on the Platinum Cathode. *Bull. Chem. Soc. Jpn.* **1963**, *36*, 53–57.
- (28) Yang, X.; Karnbach, F.; Uhlemann, M.; Odenbach, S.; Eckert, K. Dynamics of Single Hydrogen Bubbles at a Platinum Microelectrode. *Langmuir* **2015**, *31*, 8184–8193.
- (29) Westerheide, D. E.; Westwater, J. Isothermal Growth of Hydrogen Bubbles during Electrolysis. *AIChE J.* **1961**, *7*, 357–362.
- (30) Lubetkin, S. D. Why Is It Much Easier To Nucleate Gas Bubbles than Theory Predicts? *Langmuir* **2003**, *19*, 2575–2587.
- (31) Bard, A. J.; Faulkner, L. R. *Electrochemical Methods: Fundamentals and Applications*; Wiley: New York, 1980; Vol. 2.
- (32) Chen, Q.; Luo, L.; Faraji, H.; Feldberg, S. W.; White, H. S. Electrochemical Measurements of Single H₂ Nanobubble Nucleation and Stability at Pt Nanoelectrodes. *J. Phys. Chem. Lett.* **2014**, *5*, 3539–3544.
- (33) Chen, Q.; Luo, L.; White, H. S. Electrochemical Generation of a Hydrogen Bubble at a Recessed Platinum Nanopore Electrode. *Langmuir* **2015**, *31*, 4573–4581.
- (34) Chen, Q.; Wiedenroth, H. S.; German, S. R.; White, H. S. Electrochemical Nucleation of Stable N₂ Nanobubbles at Pt Nanoelectrodes. *J. Am. Chem. Soc.* **2015**, *137*, 12064–12069.
- (35) Ren, H.; German, S. R.; Edwards, M. A.; Chen, Q.; White, H. S. Electrochemical Generation of Individual O₂ Nanobubbles via H₂O₂ Oxidation. *J. Phys. Chem. Lett.* **2017**, *8*, 2450–2454.
- (36) Chen, Q.; Luo, L. Correlation between Gas Bubble Formation and Hydrogen Evolution Reaction Kinetics at Nanoelectrodes. *Langmuir* **2018**, *34*, 4554–4559.
- (37) Chen, Q.; Ranaweera, T.; Luo, L. Hydrogen Bubble Formation at Hydrogen-Insertion Electrodes. *J. Phys. Chem. C* **2018**, *122*, 15421–15426.
- (38) Liu, Y.; Edwards, M. A.; German, S. R.; Chen, Q.; White, H. S. The Dynamic Steady State of an Electrochemically Generated Nanobubble. *Langmuir* **2017**, *33*, 1845–1853.
- (39) Moreno Soto, A.; German, S. R.; Ren, H.; Van Der Meer, D.; Lohse, D.; Edwards, M. A.; White, H. S. The Nucleation Rate of Single O₂ Nanobubbles at Pt Nanoelectrodes. *Langmuir* **2018**, *34*, 7309–7318.
- (40) Navrotsky, A. Energetic Clues to Pathways to Biomineralization: Precursors, Clusters, and Nanoparticles. *Proc. Natl. Acad. Sci. U. S. A.* **2004**, *101*, 12096–12101.
- (41) Savage, J.; Dinsmore, A. Experimental Evidence for Two-Step Nucleation in Colloidal Crystallization. *Phys. Rev. Lett.* **2009**, *102*, 198302.
- (42) Brandon, N. P. *The Growth Kinetics and Interfacial Properties of Electrogenerated Bubbles*; Imperial College: London, 1985.
- (43) Brandon, N. P.; Kelsall, G. H. Growth Kinetics of Bubbles Electrogenerated at Microelectrodes. *J. Appl. Electrochem.* **1985**, *15*, 475–484.
- (44) Enríquez, O. R.; Sun, C.; Lohse, D.; Prosperetti, A.; van der Meer, D. The Quasi-Static Growth of CO₂ Bubbles. *J. Fluid Mech.* **2014**, *741*, DOI: 10.1017/jfm.2013.667.
- (45) Matsushima, H.; Kiuchi, D.; Fukunaka, Y.; Kuribayashi, K. Single Bubble Growth During Water Electrolysis Under Microgravity. *Electrochem. Commun.* **2009**, *11*, 1721–1723.
- (46) Matsushima, H.; Iida, T.; Fukunaka, Y. Gas Bubble Evolution on Transparent Electrode During Water Electrolysis in a Magnetic Field. *Electrochim. Acta* **2013**, *100*, 261–264.

- (47) Eigeldinger, J.; Vogt, H. The Bubble Coverage of Gas-Evolving Electrodes in a Flowing Electrolyte. *Electrochim. Acta* **2000**, *45*, 4449–4456.
- (48) German, S. R.; Chen, Q.; Edwards, M. A.; White, H. S. Electrochemical Measurement of Hydrogen and Nitrogen Nanobubble Lifetimes at Pt Nanoelectrodes. *J. Electrochem. Soc.* **2016**, *163*, H3160–H3166.
- (49) Craig, V. S. J.; Ninham, B. W.; Pashley, R. M. Effect of Electrolytes on Bubble Coalescence. *Nature* **1993**, *364*, 317–319.
- (50) Lessard, R. R.; Zieminski, S. A. Bubble Coalescence and Gas Transfer in Aqueous Electrolytic Solutions. *Ind. Eng. Chem. Fundam.* **1971**, *10*, 260–269.
- (51) Craig, V. S. J. Bubble Coalescence and Specific-Ion Effects. *Curr. Opin. Colloid Interface Sci.* **2004**, *9*, 178–184.
- (52) Craig, V. S. J.; Ninham, B. W.; Pashley, R. M. The Effect of Electrolytes on Bubble Coalescence in Water. *J. Phys. Chem.* **1993**, *97*, 10192–10197.
- (53) Monzon, L. M. A.; Gillen, A. J.; Mobius, M. E.; Coey, J. M. D. Effect of Tetraalkylammonium Cations on Gas Coalescence at a Hydrogen-Evolving Microelectrode. *Langmuir* **2015**, *31*, 5738–5747.
- (54) Moreno Soto, A.; Maddalena, T.; Fraters, A.; Van Der Meer, D.; Lohse, D. Coalescence of Diffusively Growing Gas Bubbles. *J. Fluid Mech.* **2018**, *846*, 143–165.
- (55) Paulsen, J. D.; Burton, J. C.; Nagel, S. R. Viscous to Inertial Crossover in Liquid Drop Coalescence. *Phys. Rev. Lett.* **2011**, *106*, 114501.
- (56) Oguz, H. N.; Prosperetti, A. Dynamics of Bubble Growth and Detachment from a Needle. *J. Fluid Mech.* **1993**, *257*, 111–145.
- (57) Schmidt, L. E.; Keim, N. C.; Zhang, W. W.; Nagel, S. R. Memory-Encoding Vibrations in a Disconnecting Air Bubble. *Nat. Phys.* **2009**, *5*, 343–346.
- (58) Huet, F.; Musiani, M.; Nogueira, R. P. Oxygen Evolution on Electrodes of Different Roughness: An Electrochemical Noise Study. *J. Solid State Electrochem.* **2004**, *8*, 786–793.
- (59) Bertocci, U.; Gabrielli, C.; Huet, F.; Keddam, M.; Rousseau, P. Noise Resistance Applied to Corrosion Measurements ii. Experimental Tests. *J. Electrochem. Soc.* **1997**, *144*, 37–43.
- (60) Lv, P.; Le The, H.; Eijkel, J.; Van den Berg, A.; Zhang, X.; Lohse, D. Growth and Detachment of Oxygen Bubbles Induced by Gold-Catalyzed Decomposition of Hydrogen Peroxide. *J. Phys. Chem. C* **2017**, *121*, 20769–20776.
- (61) van Helden, W. G. J. *On Detaching Bubbles in Upward Flow Boiling*; Technische Universiteit Eindhoven: Eindhoven, The Netherlands, 1994.
- (62) Brandon, N. P.; Kelsall, G. H.; Levine, S.; Smith, A. L. Interfacial Electrical Properties of Electrogenerated Bubbles. *J. Appl. Electrochem.* **1985**, *15*, 485–493.
- (63) Kelsall, G. H.; Tang, S.; Yurdakul, S.; Smith, A. L. Electrophoretic Behaviour of Bubbles in Aqueous Electrolytes. *J. Chem. Soc., Faraday Trans.* **1996**, *92*, 3887–3893.
- (64) Bode, D. D., Jr.; Andersen, T. N.; Eyring, H. Anion and pH Effects on the Potentials of Zero Charge of Gold and Silver Electrodes. *J. Phys. Chem.* **1967**, *71*, 792–797.
- (65) Lubetkin, S. D. The Fundamentals of Bubble Evolution. *Chem. Soc. Rev.* **1995**, *24*, 243–250.
- (66) Fernandez, D.; Maurer, P.; Martine, M.; Coey, J. M. D.; Möbius, M. E. Bubble Formation at a Gas-Evolving Microelectrode. *Langmuir* **2014**, *30*, 13065–13074.
- (67) Baczyzmalski, D.; Karnbach, F.; Mutschke, G.; Yang, X.; Eckert, K.; Uhlemann, M.; Cierpka, C. Growth and Detachment of Single Hydrogen Bubbles in a Magnetohydrodynamic Shear Flow. *Phys. Rev. Fluids* **2017**, *2*, 093701.
- (68) Monzon, L. M. A.; Coey, J. M. D. Magnetic Fields in Electrochemistry: The Lorentz Force. A Mini-Review. *Electrochem. Commun.* **2014**, *42*, 38–41.
- (69) Fernández, D.; Martine, M.; Meagher, A.; Möbius, M. E.; Coey, J. M. D. Stabilizing Effect of A Magnetic Field on A Gas Bubble Produced at A Microelectrode. *Electrochem. Commun.* **2012**, *18*, 28–32.
- (70) Cherian, C. T.; Giustiniano, F.; Martin Fernandez, I.; Andersen, H.; Balakrishnan, J.; Özyilmaz, B. ‘Bubble Free’ Electrochemical Delamination of CVD Graphene Films. *Small* **2015**, *11*, 189–194.
- (71) Mixon, F. O., Jr.; Chon, W. Y.; Beatty, K. O., Jr. The Effect of Electrolytic Gas Evolution on Heat Transfer. *Chem. Eng. Progr.* **1960**, *56*.
- (72) Blandamer, M. J.; Franks, F.; Haywood, K. H.; Tory, A. C. Effect of Added Solutes on the Size of Hydrogen Bubbles Liberated from a Cathodic Wire in Aqueous Solution. *Nature* **1967**, *216*, 783–784.
- (73) Dukovic, J.; Tobias, C. W. The Influence of Attached Bubbles on Potential Drop and Current Distribution at Gas Evolving Electrodes. *J. Electrochem. Soc.* **1987**, *134*, 331–343.
- (74) Vogt, H. The Concentration Overpotential of Gas Evolving Electrodes as a Multiple Problem of Mass Transfer. *J. Electrochem. Soc.* **1990**, *137*, 1179–1184.
- (75) Vogt, H. Mass Transfer at Gas Evolving Electrodes with Superposition of Hydrodynamic Flow. *Electrochim. Acta* **1978**, *23*, 203–205.
- (76) Gabrielli, C.; Huet, F.; Nogueira, R. P. Fluctuations of Concentration Overpotential Generated at Gas-Evolving Electrodes. *Electrochim. Acta* **2005**, *50*, 3726–3736.
- (77) Gabrielli, C.; Huet, F.; Keddam, M.; Macias, A.; Sahar, A. Potential Drops due to an Attached Bubble on a Gas-Evolving Electrode. *J. Appl. Electrochem.* **1989**, *19*, 617–629.
- (78) Vogt, H. The Actual Current Density of Gas-Evolving Electrodes-Notes on the Bubble Coverage. *Electrochim. Acta* **2012**, *78*, 183–187.
- (79) Vogt, H.; Balzer, R. J. The Bubble Coverage of Gas-Evolving Electrodes in Stagnant Electrolytes. *Electrochim. Acta* **2005**, *50*, 2073–2079.
- (80) Darby, R.; Haque, M. The Dynamics of Electrolytic Hydrogen Bubble Evolution. *Chem. Eng. Sci.* **1973**, *28*, 1129–1138.
- (81) Sillen, C. W. M. P.; Barendrecht, E.; Janssen, L. J. J.; van Stralen, S. J. D. In *Gas Bubble Behaviour during Water Electrolysis*; Strub, A. A., Imarisio, G., Eds.; Hydrogen as an Energy Vector; Springer: Dordrecht, The Netherlands, 1980; pp 328–348.
- (82) Bryson, A.; Hofman, D. A Population Balance Approach to the Study of Bubble Behaviour at Gas-Evolving Electrodes. *J. Appl. Electrochem.* **1989**, *19*, 116–119.
- (83) Janssen, L. J. J.; Van Stralen, S. J. D. Bubble Behaviour on and Mass transfer to an Oxygen-Evolving Transparent Nickel Electrode in Alkaline Solution. *Electrochim. Acta* **1981**, *26*, 1011–1022.
- (84) Balzer, R. J.; Vogt, H. Effect of Electrolyte Flow on the Bubble Coverage of Vertical Gas-Evolving Electrodes. *J. Electrochem. Soc.* **2003**, *150*, E11–E16.
- (85) Vogt, H. The Quantities Affecting the Bubble Coverage of Gas-Evolving Electrodes. *Electrochim. Acta* **2017**, *235*, 495–499.
- (86) Janssen, L. J. J.; Sillen, C. W. M. P.; Barendrecht, E.; Van Stralen, S. J. D. Bubble Behaviour During Oxygen and Hydrogen Evolution at Transparent Electrodes in KOH Solution. *Electrochim. Acta* **1984**, *29*, 633–642.
- (87) Leistra, J. A.; Sides, P. J. Voltage Components at Gas Evolving Electrodes. *J. Electrochem. Soc.* **1987**, *134*, 2442–2446.
- (88) Sides, P. J.; Tobias, C. W. Primary Potential and Current Distribution Around a Bubble on an Electrode. *J. Electrochem. Soc.* **1980**, *127*, 288–291.
- (89) Sides, P. J.; Tobias, C. W. Resistance of a Planar Array of Spheres: Gas Bubbles on an Electrode. *J. Electrochem. Soc.* **1982**, *129*, 2715–2720.
- (90) Gabrielli, C.; Huet, F.; Keddam, M.; Sahar, A. Investigation of Water Electrolysis by Spectral Analysis. I. Influence of the Current Density. *J. Appl. Electrochem.* **1989**, *19*, 683–696.
- (91) Sides, P. J. Phenomena and Effects of Electrolytic Gas Evolution. *Modern Aspects of Electrochemistry*; Springer: 1986; pp 303–354.
- (92) Banisi, S.; Finch, J. A.; Laplante, A. R. Electrical Conductivity of Dispersions: A Review. *Miner. Eng.* **1993**, *6*, 369–385.

- (93) Maxwell, J. C. *A Treatise on Electricity and Magnetism*; Clarendon Press: 1881; Vol. 1.
- (94) Jeffrey, D. J. Conduction Through a Random Suspension of Spheres. *Proc. R. Soc. London, Ser. A* **1973**, *335*, 355–367.
- (95) Prager, S. Diffusion and Viscous Flow in Concentrated Suspensions. *Physica* **1963**, *29*, 129–139.
- (96) Meredith, R. E.; Tobias, C. W. Conductivities in Emulsions. *J. Electrochem. Soc.* **1961**, *108*, 286–290.
- (97) Bruggeman, V. D. Berechnung verschiedener physikalischer Konstanten von heterogenen Substanzen. I. Dielektrizitätskonstanten und Leitfähigkeiten der Mischkörper aus isotropen Substanzen. *Ann. Phys.* **1935**, *416*, 636–664.
- (98) De La Rue, R. E.; Tobias, C. W. On the Conductivity of Dispersions. *J. Electrochem. Soc.* **1959**, *106*, 827–833.
- (99) Neale, G. H.; Nader, W. K. Prediction of Transport Processes within Porous Media: Diffusive Flow Processes within a Homogeneous Swarm of Spherical Particles. *AIChE J.* **1973**, *19*, 112–119.
- (100) Clark, N. The Electrical Conductivity of Foam. *Trans. Faraday Soc.* **1948**, *44*, 13–15.
- (101) Tobias, C. W. Effect of Gas Evolution on Current Distribution and Ohmic Resistance in Electrolyzers. *J. Electrochem. Soc.* **1959**, *106*, 833–838.
- (102) Bongenaar-Schlenter, B. E.; Janssen, L. J. J.; Van Stralen, S. J. D.; Barendrecht, E. The Effect of the Gas Void Distribution on the Ohmic Resistance during Water Electrolytes. *J. Appl. Electrochem.* **1985**, *15*, 537–548.
- (103) Krause, B.; Vogt, H. Effect of Operational Parameters on Gas Evolution in Electrolyte Bulk: Possibilities for Lowering Interelectrode Resistance. *J. Appl. Electrochem.* **1985**, *15*, 509–515.
- (104) Vogt, H. The Voidage Problem in Gas-Electrolyte Dispersions. *J. Appl. Electrochem.* **1987**, *17*, 419–426.
- (105) Vogt, H. A Hydrodynamic Model for the Ohmic Interelectrode Resistance of Cells with Vertical Gas Evolving Electrodes. *Electrochim. Acta* **1981**, *26*, 1311–1317.
- (106) Janssen, L. J. J.; Visser, G. J. Behaviour of a Tall Vertical Gas-Evolving Cell. Part I: Distribution of Void Fraction and of Ohmic Resistance. *J. Appl. Electrochem.* **1991**, *21*, 386–394.
- (107) Weijs, M. P. M. G.; Janssen, L. J. J.; Visser, G. J. Ohmic Resistance of Solution in a Vertical Gas-Evolving Cell. *J. Appl. Electrochem.* **1997**, *27*, 371–378.
- (108) Kreysa, G.; Kùlps, H. J. Experimental Study of the Gas Bubble Effects on the IR Drop at Inclined Electrodes. *J. Electrochem. Soc.* **1981**, *128*, 979–984.
- (109) Kreysa, G.; Kuhn, M. Modelling of Gas Evolving Electrolysis Cells. I. The Gas Voidage Problem. *J. Appl. Electrochem.* **1985**, *15*, 517–526.
- (110) Kuhn, M.; Kreysa, G. Modelling of Gas-Evolving Electrolysis Cells. III. The iR Drop at Gas-Evolving Electrodes. *J. Appl. Electrochem.* **1989**, *19*, 720–728.
- (111) Lanzi, O.; Savinell, R. F. A Modified Constriction Model for the Resistivity of a Bubble Curtain on a Gas Evolving Electrode. *J. Electrochem. Soc.* **1983**, *130*, 799–802.
- (112) Philippe, M.; Jérôme, H.; Sebastien, B.; Gérard, P. Modelling and Calculation of the Current Density Distribution Evolution at Vertical Gas-Evolving Electrodes. *Electrochim. Acta* **2005**, *51*, 1140–1156.
- (113) Mandin, P.; Derhouni, Z.; Roustan, H.; Rolf, W. Bubble Over-Potential During Two-Phase Alkaline Water Electrolysis. *Electrochim. Acta* **2014**, *128*, 248–258.
- (114) Janssen, L. J. J.; Geraets, J. J. M.; Barendrecht, E.; Van Stralen, S. D. J. Ohmic Potential Drop During Alkaline Water Electrolysis. *Electrochim. Acta* **1982**, *27*, 1207–1218.
- (115) Roušar, I.; Cezner, V. Transfer of Mass or Heat to An Electrode in the Region of Hydrogen Evolution—I Theory. *Electrochim. Acta* **1975**, *20*, 289–293.
- (116) Roušar, I.; Kačín, J.; Lippert, E.; Šmirous, F.; Cezner, V. Transfer of Mass or Heat to An Electrode in the Region of Hydrogen Evolution—II.: Experimental Verification of Mass and Heat Transfer Equations. *Electrochim. Acta* **1975**, *20*, 295–299.
- (117) Vogt, H. Heat Transfer at Gas Evolving Electrodes. *Electrochim. Acta* **1978**, *23*, 1019–1022.
- (118) Fouad, M. G.; Sedahmed, G. H. Mass Transfer at Horizontal Gas-Evolving Electrodes. *Electrochim. Acta* **1973**, *18*, 55–58.
- (119) Fouad, M. G.; Sedahmed, G. H. Mass Transfer at Gas Evolving Screen Electrodes. *Electrochim. Acta* **1975**, *20*, 615–618.
- (120) Fouad, M.; Sedahmed, G. Effect of Gas Evolution on the Rate of Mass Transfer at Vertical Electrodes. *Electrochim. Acta* **1972**, *17*, 665–672.
- (121) Janssen, L. J. J. Mass Transfer at Gas Evolving Electrodes. *Electrochim. Acta* **1978**, *23*, 81–86.
- (122) Janssen, L. J. J.; Hoogland, J. G. The Effect of Electrolytically Evolved Gas Bubbles on the Thickness of the Diffusion Layer. *Electrochim. Acta* **1970**, *15*, 1013–1023.
- (123) Janssen, L. J. J.; Hoogland, J. G. The Effect of Electrolytically Evolved Gas Bubbles on the Thickness of the Diffusion Layer—II. *Electrochim. Acta* **1973**, *18*, 543–550.
- (124) El-Sherbiny, M.; Zatout, A.; Hussien, M.; Sedahmed, G. Mass Transfer at the Gas Evolving Inner Electrode of a Concentric Cylindrical Reactor. *J. Appl. Electrochem.* **1991**, *21*, 537–542.
- (125) Sedahmed, G. H. Mass Transfer at Packed-Bed, Gas-Evolving Electrodes. *J. Appl. Electrochem.* **1987**, *17*, 746–752.
- (126) Janssen, L. J. J.; Barendrecht, E. Mechanism of Mass Transfer of Indicator Ions to an Oxygen-Evolving and a Hydrogen-Evolving Electrode in Alkaline Solution. *Electrochim. Acta* **1985**, *30*, 683–694.
- (127) Green, M.; Robinson, P. H. Kinetics of the Cathodic Reduction of Anions: Germanium Oxides. *J. Electrochem. Soc.* **1959**, *106*, 253–260.
- (128) Beck, T. A Contribution to the Theory of Electrolytic Chlorate Formation. *J. Electrochem. Soc.* **1969**, *116*, 1038–1041.
- (129) Vogt, H. Gas-Evolving Electrodes. *Comprehensive Treatise of Electrochemistry*; Springer: 1983; pp 445–489.
- (130) Ibl, N.; Venczel, J.; Schalch, E. Stofftransport bei der Elektrolyse mit Gasrührung. *Chem. Ing. Tech.* **1971**, *43*, 202–215.
- (131) Stephan, K.; Vogt, H. A Model for Correlating Mass Transfer Data at Gas Evolving Electrodes. *Electrochim. Acta* **1979**, *24*, 11–18.
- (132) Vogt, H.; Stephan, K. Local Microprocesses at Gas-Evolving Electrodes and their Influence on Mass Transfer. *Electrochim. Acta* **2015**, *155*, 348–356.
- (133) Hreiz, R.; Abdelouahed, L.; Fuenfchilling, D.; Lopicque, F. Electrogenerated Bubbles Induced Convection in Narrow Vertical Cells: A Review. *Chem. Eng. Res. Des.* **2015**, *100*, 268–281.
- (134) Taqieddin, A.; Nazari, R.; Rajic, L.; Alshawabkeh, A. Physicochemical Hydrodynamics of Gas Bubbles in Two Phase Electrochemical Systems. *J. Electrochem. Soc.* **2017**, *164*, E448–E459.
- (135) Yang, X.; Baczyzmalski, D.; Cierpka, C.; Mutschke, G.; Eckert, K. Marangoni Convection at Electrogenerated Hydrogen Bubbles. *Phys. Chem. Chem. Phys.* **2018**, *20*, 11542–11548.
- (136) Massing, J.; Mutschke, G.; Baczyzmalski, D.; Hossain, S. S.; Yang, X.; Eckert, K.; Cierpka, C. Thermocapillary convection during hydrogen evolution at microelectrodes. *Electrochim. Acta* **2019**, *297*, 929–940.
- (137) Zhang, J.; Sasaki, K.; Sutter, E.; Adzic, R. R. Stabilization of Platinum Oxygen-Reduction Electrocatalysts Using Gold Clusters. *Science* **2007**, *315*, 220–222.
- (138) Hu, J.; Wu, L.; Kuttiyiel, K. A.; Goodman, K. R.; Zhang, C.; Zhu, Y.; Vukmirovic, M. B.; White, M. G.; Sasaki, K.; Adzic, R. R. Increasing Stability and Activity of Core-Shell Catalysts by Preferential Segregation of Oxide on Edges and Vertices: Oxygen Reduction on Ti–Au@Pt/C. *J. Am. Chem. Soc.* **2016**, *138*, 9294–9300.
- (139) Geiger, S.; Kasian, O.; Ledendecker, M.; Pizzutilo, E.; Mingers, A. M.; Fu, W. T.; Diaz-Morales, O.; Li, Z.; Oellers, T.; Fruchter, L.; et al. The Stability Number as a Metric for Electrocatalyst Stability Benchmarking. *Nat. Catal.* **2018**, *1*, 508–515.
- (140) Faber, M. S.; Dziedzic, R.; Lukowski, M. A.; Kaiser, N. S.; Ding, Q.; Jin, S. High-Performance Electrocatalysis Using Metallic Cobalt Pyrite (CoS₂) Micro- and Nanostructures. *J. Am. Chem. Soc.* **2014**, *136*, 10053–10061.

- (141) Goryachev, V. L.; Ufimtsev, A. A.; Khodakovskii, A. M. Mechanism of Electrode Erosion in Pulsed Discharges in Water with a Pulse Energy of ~ 1 J. *Tech. Phys. Lett.* **1997**, *23*, 386–387.
- (142) Zhao, X.; Ranaweera, R.; Luo, L. Highly Efficient Hydrogen Evolution of Platinum via Tuning the Interfacial Dissolved-Gas Concentration. *Chem. Commun.* **2019**, *55*, 1378–1381.
- (143) Mazloomi, S. K.; Sulaiman, N. Influencing Factors of Water Electrolysis Electrical Efficiency. *Renewable Sustainable Energy Rev.* **2012**, *16*, 4257–4263.
- (144) Mao, S.; Wen, Z.; Huang, T.; Hou, Y.; Chen, J. High-Performance Bi-functional Electrocatalysts of 3D Crumpled Graphene-Cobalt Oxide Nanohybrids for Oxygen Reduction and Evolution Reactions. *Energy Environ. Sci.* **2014**, *7*, 609–616.
- (145) Sun, H.; Xu, X.; Yan, Z.; Chen, X.; Jiao, L.; Cheng, F.; Chen, J. Superhydrophilic Amorphous Co-B-P Nanosheet Electrocatalysts with Pt-like Activity and Durability for the Hydrogen Evolution Reaction. *J. Mater. Chem. A* **2018**, *6*, 22062–22069.
- (146) Wang, M.; Wang, Z.; Gong, X.; Guo, Z. The Intensification Technologies to Water Electrolysis for Hydrogen Production - A Review. *Renewable Sustainable Energy Rev.* **2014**, *29*, 573–588.
- (147) Sui, C.; Chen, K.; Zhao, L.; Zhou, L.; Wang, Q.-Q. MoS₂-Modified Porous Gas Diffusion Layer with Air-Solid-Liquid Interface for Efficient Electrocatalytic Water Splitting. *Nanoscale* **2018**, *10*, 15324–15331.
- (148) Darband, G. B.; Aliofkhaezai, M.; Rouhaghdam, A. S.; Kiani, M. Three-Dimensional Ni-Co Alloy Hierarchical Nanostructure as Efficient Non-Noble-Metal Electrocatalyst for Hydrogen Evolution Reaction. *Appl. Surf. Sci.* **2019**, *465*, 846–862.
- (149) Lu, Z.; Zhu, W.; Yu, X.; Zhang, H.; Li, Y.; Sun, X.; Wang, X.; Wang, H.; Wang, J.; Luo, J.; et al. Ultrahigh Hydrogen Evolution Performance of Under Water “Superaerophobic” MoS₂ Nanostructured Electrodes. *Adv. Mater.* **2014**, *26*, 2683–2687.
- (150) Xu, W.; Lu, Z.; Sun, X.; Jiang, L.; Duan, X. Superwetting Electrodes for Gas-Involving Electrocatalysis. *Acc. Chem. Res.* **2018**, *51*, 1590–1598.
- (151) Xu, W.; Lu, Z.; Wan, P.; Kuang, Y.; Sun, X. High Performance Water Electrolysis System with Double Nanostructured Superaerophobic Electrodes. *Small* **2016**, *12*, 2492–2498.
- (152) Jiang, M.; Wang, H.; Li, Y.; Zhang, H.; Zhang, G.; Lu, Z.; Sun, X.; Jiang, L. Superaerophobic RuO₂ Based Nanostructured Electrode for High Performance Chlorine Evolution Reaction. *Small* **2017**, *13*, 1602240.
- (153) Lu, Z.; Sun, M.; Xu, T.; Li, Y.; Xu, W.; Chang, Z.; Ding, Y.; Sun, X.; Jiang, L. Superaerophobic Electrodes for Direct Hydrazine Fuel Cells. *Adv. Mater.* **2015**, *27*, 2361–2366.
- (154) Kuang, Y.; Feng, G.; Li, P.; Bi, Y.; Li, Y.; Sun, X. Single Crystalline Ultrathin Nickel Nanosheets Array from In Situ Topotactic Reduction for Active and Stable Electrocatalysis. *Angew. Chem., Int. Ed.* **2016**, *55*, 693–697.
- (155) Feng, G.; Kuang, Y.; Li, Y.; Sun, X. Three-Dimensional Porous Superaerophobic Nickel Nanoflower Electrodes for High-Performance Hydrazine Oxidation. *Nano Res.* **2015**, *8*, 3365–3371.
- (156) He, J.; Hu, B.; Zhao, Y. Superaerophobic Electrode with Metal@ Metal Oxide Powder Catalyst for Oxygen Evolution Reaction. *Adv. Funct. Mater.* **2016**, *26*, 5998–6004.
- (157) Yan, Y.; Xia, B.; Li, N.; Xu, Z.; Fisher, A.; Wang, X. Vertically Oriented MoS₂ and WS₂ Nanosheets Directly Grown on Carbon Cloth as Efficient and Stable 3-Dimensional Hydrogen-Evolving Cathodes. *J. Mater. Chem. A* **2015**, *3*, 131–135.
- (158) Hao, J.; Yang, W.; Huang, Z.; Zhang, C. Superhydrophilic and Superaerophobic Copper Phosphide Microsheets for Efficient Electrocatalytic Hydrogen and Oxygen Evolution. *Adv. Mater. Interfaces* **2016**, *3*, 1600236.
- (159) Cheng, Z.; Gao, J.; Fu, Q.; Li, C.; Wang, X.; Xiao, Y.; Zhao, Y.; Zhang, Z.; Qu, L. Interconnected Molybdenum Carbide-Based Nanoribbons for Highly Efficient and Ultrastable Hydrogen Evolution. *ACS Appl. Mater. Interfaces* **2017**, *9*, 24608–24615.
- (160) Akbar, K.; Hussain, S.; Truong, L.; Roy, S. B.; Jeon, J. H.; Jerng, S.-K.; Kim, M.; Yi, Y.; Jung, J.; Chun, S.-H. Induced Superaerophobicity onto a Non-superaerophobic Catalytic Surface for Enhanced Hydrogen Evolution Reaction. *ACS Appl. Mater. Interfaces* **2017**, *9*, 43674–43680.
- (161) Wang, L.; Huang, X.; Jiang, S.; Li, M.; Zhang, K.; Yan, Y.; Zhang, H.; Xue, J. M. Increasing Gas Bubble Escape Rate for Water Splitting with Nonwoven Stainless Steel Fabrics. *ACS Appl. Mater. Interfaces* **2017**, *9*, 40281–40289.
- (162) Li, Y.; Zhang, H.; Xu, T.; Lu, Z.; Wu, X.; Wan, P.; Sun, X.; Jiang, L. Under Water Superaerophobic Pine Shaped Pt Nanoray Electrode for Ultrahigh Performance Hydrogen Evolution. *Adv. Funct. Mater.* **2015**, *25*, 1737–1744.
- (163) Burdyny, T.; Graham, P. J.; Pang, Y.; Dinh, C.-T.; Liu, M.; Sargent, E. H.; Sinton, D. Nanomorphology-Enhanced Gas-Evolution Intensifies CO₂ Reduction Electrochemistry. *ACS Sustainable Chem. Eng.* **2017**, *5*, 4031–4040.
- (164) Shin, H. C.; Dong, J.; Liu, M. Nanoporous Structures Prepared by an Electrochemical Deposition Process. *Adv. Mater.* **2003**, *15*, 1610–1614.
- (165) Shin, H.-C.; Liu, M. Copper Foam Structures with Highly Porous Nanostructured Walls. *Chem. Mater.* **2004**, *16*, 5460–5464.
- (166) Li, Y.; Jia, W.-Z.; Song, Y.-Y.; Xia, X.-H. Superhydrophobicity of 3D Porous Copper Films Prepared Using the Hydrogen Bubble Dynamic Template. *Chem. Mater.* **2007**, *19*, 5758–5764.
- (167) Li, Y.; Song, Y.-Y.; Yang, C.; Xia, X.-H. Hydrogen Bubble Dynamic Template Synthesis of Porous Gold for Nonenzymatic Electrochemical Detection of Glucose. *Electrochem. Commun.* **2007**, *9*, 981–988.
- (168) González-Buch, C.; Herráiz-Cardona, I.; Ortega, E.; García-Antón, J.; Pérez-Herranz, V. Synthesis and Characterization of Macroporous Ni, Co and Ni-Co Electrocatalytic Deposits for Hydrogen Evolution Reaction in Alkaline Media. *Int. J. Hydrogen Energy* **2013**, *38*, 10157–10169.
- (169) Cherevko, S.; Xing, X.; Chung, C.-H. Electrodeposition of Three-Dimensional Porous Silver Foams. *Electrochem. Commun.* **2010**, *12*, 467–470.
- (170) Cherevko, S.; Kulyk, N.; Chung, C.-H. Nanoporous Palladium with Sub-10 nm Dendrites by Electrodeposition for Ethanol and Ethylene Glycol Oxidation. *Nanoscale* **2012**, *4*, 103–105.
- (171) Ott, A.; Jones, L. A.; Bhargava, S. K. Direct Electrodeposition of Porous Platinum Honeycomb Structures. *Electrochem. Commun.* **2011**, *13*, 1248–1251.
- (172) Yang, M. Fern-Shaped Bismuth Dendrites Electrodeposited at Hydrogen Evolution Potentials. *J. Mater. Chem.* **2011**, *21*, 3119–3124.
- (173) Oppedisano, D. K.; Jones, L. A.; Junk, T.; Bhargava, S. K. Ruthenium Electrodeposition from Aqueous Solution at High Cathodic Overpotential. *J. Electrochem. Soc.* **2014**, *161*, D489–D494.
- (174) Yu, X.; Wang, M.; Wang, Z.; Gong, X.; Guo, Z. 3D Multi-structural Porous NiAg Films with Nanoarchitecture Walls: High Catalytic Activity and Stability for Hydrogen Evolution Reaction. *Electrochim. Acta* **2016**, *211*, 900–910.
- (175) Rafailović, L. D.; Minić, D. M.; Karnthaler, H. P.; Wosik, J.; Trišović, T.; Nauer, G. E. Study of the Dendritic Growth of Ni-Co Alloys Electrodeposited on Cu Substrates. *J. Electrochem. Soc.* **2010**, *157*, D295–D301.
- (176) Zhuo, K.; Jeong, M.-G.; Chung, C.-H. Highly Porous Dendritic Ni-Sn Anodes for Lithium-Ion Batteries. *J. Power Sources* **2013**, *244*, 601–605.
- (177) Rafailović, L. D.; Gammer, C.; Kleber, C.; Rentenberger, C.; Angerer, P.; Karnthaler, H. P. Synthesis and Characterization of Electrodeposited Hierarchical Nanodendritic NiCoFe Alloy Powders. *J. Alloys Compd.* **2012**, *543*, 167–171.
- (178) Mattarozzi, L.; Cattarin, S.; Comisso, N.; Gambirasi, A.; Guerriero, P.; Musiani, M.; Vázquez-Gómez, L.; Verlatto, E. Hydrogen Evolution Assisted Electrodeposition of Porous Cu-Ni Alloy Electrodes and their Use for Nitrate Reduction in Alkali. *Electrochim. Acta* **2014**, *140*, 337–344.
- (179) Mattarozzi, L.; Cattarin, S.; Comisso, N.; Gerbasi, R.; Guerriero, P.; Musiani, M.; Verlatto, E. Electrodeposition of Compact

and Porous Cu-Pd Alloy Layers and Their Application to Nitrate Reduction in Alkali. *Electrochim. Acta* **2017**, *230*, 365–372.

(180) Najdovski, I.; Selvakannan, P.; Bhargava, S. K.; O'Mullane, A. P. Formation of Nanostructured Porous Cu-Au Surface: the Influence of Cationic Sites on (Electro)-catalysis. *Nanoscale* **2012**, *4*, 6298–6306.

(181) Cherevko, S.; Kulyk, N.; Chung, C.-H. Pulse-Reverse Electrodeposition for Mesoporous Metal Films: Combination of Hydrogen Evolution Assisted Deposition and Electrochemical Dealloying. *Nanoscale* **2012**, *4*, 568–575.

(182) Liu, J.; Cao, L.; Huang, W.; Li, Z. Preparation of AuPt Alloy Foam Films and Their Superior Electrocatalytic Activity for the Oxidation of Formic Acid. *ACS Appl. Mater. Interfaces* **2011**, *3*, 3552–3558.

(183) Li, R.; Mao, H.; Zhang, J.; Huang, T.; Yu, A. Rapid Synthesis of Porous Pd and PdNi Catalysts using Hydrogen Bubble Dynamic Template and their Enhanced Catalytic Performance for Methanol Electrooxidation. *J. Power Sources* **2013**, *241*, 660–667.

(184) Niu, X.; Zhao, H.; Chen, C.; Lan, M. Enhancing the Electrocatalytic Activity of Pt–Pd Catalysts by Introducing Porous Architectures. *ChemCatChem* **2013**, *5*, 1416–1425.

(185) Comisso, N.; Cattarin, S.; Guerriero, P.; Mattarozzi, L.; Musiani, M.; Verlati, E. Electrochemical Behaviour of Porous PbO₂ Layers Prepared by Oxygen Bubble Templated Anodic Deposition. *Electrochim. Acta* **2016**, *200*, 259–267.

(186) Hu, X.; Cheng, F.; Han, X.; Zhang, T.; Chen, J. Oxygen Bubble Templated Hierarchical Porous ϵ MnO₂ as a Superior Catalyst for Rechargeable Li–O₂ Batteries. *Small* **2015**, *11*, 809–813.

(187) Yang, X.; Liu, A.; Zhao, Y.; Lu, H.; Zhang, Y.; Wei, W.; Li, Y.; Liu, S. Three-Dimensional Macroporous Polypyrrole-Derived Graphene Electrode Prepared by the Hydrogen Bubble Dynamic Template for Supercapacitors and Metal-Free Catalysts. *ACS Appl. Mater. Interfaces* **2015**, *7*, 23731–23740.

(188) Dutta, A.; Morstein, C. E.; Rahaman, M.; Cedeno López, A.; Broekmann, P. Beyond Copper in CO₂ Electrolysis: Effective Hydrocarbon Production on Silver-Nanofoam Catalysts. *ACS Catal.* **2018**, *8*, 8357–8368.

(189) Oh, S.; Kim, H.; Kwon, Y.; Kim, M.; Cho, E.; Kwon, H. Porous Co-P Foam as an Efficient Bifunctional Electrocatalyst for Hydrogen and Oxygen Evolution Reaction. *J. Mater. Chem. A* **2016**, *4*, 18272–18277.

(190) Wei, L.; Goh, K.; Birer, Ö.; Karahan, H. E.; Chang, J.; Zhai, S.; Chen, X.; Chen, Y. A Hierarchically Porous Nickel-Copper Phosphide Nano-Foam for Efficient Electrochemical Splitting of Water. *Nanoscale* **2017**, *9*, 4401–4408.

(191) Li, S.; Du, Y.; He, T.; Shen, Y.; Bai, C.; Ning, F.; Hu, X.; Wang, W.; Xi, S.; Zhou, X. Nanobubbles: An Effective Way to Study Gas-Generating Catalysis on a Single Nanoparticle. *J. Am. Chem. Soc.* **2017**, *139*, 14277–14284.

(192) Lohse, D.; Zhang, X. Surface Nanobubbles and Nanodroplets. *Rev. Mod. Phys.* **2015**, *87*, 981–1035.

(193) Zhang, X.; Lohse, D. Perspectives on Surface Nanobubbles. *Biomicrofluidics* **2014**, *8*, 041301.

(194) Weijs, J. H.; Lohse, D. Why Surface Nanobubbles Live for Hours. *Phys. Rev. Lett.* **2013**, *110*, 054501.

(195) An, H.; Liu, G.; Craig, V. S. J. Wetting of Nanophases: Nanobubbles, Nanodroplets and Micropancakes on Hydrophobic Surfaces. *Adv. Colloid Interface Sci.* **2015**, *222*, 9–17.

(196) Zhang, X.; Maeda, N. Interfacial Gaseous States on Crystalline Surfaces. *J. Phys. Chem. C* **2011**, *115*, 736–743.

(197) Zhang, X. H.; Zhang, X.; Sun, J.; Zhang, Z.; Li, G.; Fang, H.; Xiao, X.; Zeng, X.; Hu, J. Detection of Novel Gaseous States at the Highly Oriented Pyrolytic Graphite-Water Interface. *Langmuir* **2007**, *23*, 1778–1783.

(198) Chen, J. G.; Crooks, R. M.; Seefeldt, L. C.; Bren, K. L.; Bullock, R. M.; Darensbourg, M. Y.; Holland, P. L.; Hoffman, B.; Janik, M. J.; Jones, A. K.; et al. Beyond Fossil Fuel-Driven Nitrogen Transformations. *Science* **2018**, *360*, No. eaar6611.

(199) Qiao, J.; Liu, Y.; Hong, F.; Zhang, J. A Review of Catalysts for The Electroreduction of Carbon Dioxide to Produce Low-Carbon Fuels. *Chem. Soc. Rev.* **2014**, *43*, 631–675.

(200) Ganesh, I. Conversion of Carbon Dioxide into Methanol - a Potential Liquid Fuel: Fundamental Challenges and Opportunities (A Review). *Renewable Sustainable Energy Rev.* **2014**, *31*, 221–257.

(201) Lim, R. J.; Xie, M.; Sk, M. A.; Lee, J.-M.; Fisher, A.; Wang, X.; Lim, K. H. A Review on The Electrochemical Reduction of CO₂ in Fuel Cells, Metal Electrodes and Molecular Catalysts. *Catal. Today* **2014**, *233*, 169–180.

(202) Frontana-Urbe, B. A.; Little, R. D.; Ibanez, J. G.; Palma, A.; Vasquez-Medrano, R. Organic Electrosynthesis: a Promising Green Methodology in Organic Chemistry. *Green Chem.* **2010**, *12*, 2099–2119.

(203) Malik, K.; Singh, S.; Basu, S.; Verma, A. Electrochemical Reduction of CO₂ for Synthesis of Green Fuel. *WIREs Energy Environ.* **2017**, *6*, No. e244.

(204) Zheng, J. Y.; Lyu, Y. H.; Qiao, M.; Wang, R. L.; Zhou, Y. Y.; Li, H.; Chen, C.; Li, Y. F.; Zhou, H. J.; Jiang, S. P.; Wang, S. Y. Photoelectrochemical Synthesis of Ammonia on the Aerophilic-Hydrophilic Heterostructure with 37.8% Efficiency. *Chem.* **2019**, *5*, 617–633.